

# Light-controlled membrane remodeling in gel-fluid phase-separated giant vesicles using photoswitchable lipids

Tsu-Wang Sun<sup>1</sup>, Elias Sabri<sup>1</sup>, Mina Aleksanyan<sup>1</sup>, Rumiana Dimova<sup>1,\*</sup>

<sup>1</sup>Max Planck Institute of Colloids and Interfaces, 14476 Potsdam, Germany

\* Address correspondence to: [Rumiana.Dimova@mpikg.mpg.de](mailto:Rumiana.Dimova@mpikg.mpg.de)

**Keywords:** giant unilamellar vesicles (GUV), photomanipulation, lipid phase separation, membrane domain organization, azobenzene phospholipid (azoPC), domain-induced budding

## Abstract

Photoswitchable lipids enable optical control of membrane area, mechanics and phase behavior, offering a platform to study stimuli-responsive biomimetic systems. However, it remains unclear how the spatial organization of coexisting membrane phases governs photoinduced mechanical responses. Here, we incorporate the photoswitch azobenzene-phosphatidylcholine (azoPC) and dipalmitoylphosphatidylcholine (DPPC) into gel-fluid phase-separated giant unilamellar vesicles (GUVs) to probe how domain architecture controls light-driven deformation. We combine differential scanning calorimetry, temperature-controlled confocal microscopy, and a calibrated heating stage to quantify phase transitions and visualize domain dynamics. Dispersed domains produce global GUV crumpling upon UV-light-induced *trans*-to-*cis* isomerization of azoPC, whereas coarsened fluid domains locally confine deformation to budding regions of the GUVs; both responses are reversed by blue light. Temperature-controlled imaging reveals that the gel-fluid transition in GUVs is considerably broader than the calorimetric profile suggests, with coexisting phases detectable well above the calorimetry peak transition temperature. Well above the transition temperature, i.e. in the fully melted membrane, UV irradiation unexpectedly induces reversible nucleation of gel-like flower domains, consistent with an increased transition temperature in the *cis* azoPC state due to lipid packing incompatibility with DPPC. These results demonstrate that membrane domain architecture dictates the spatial distribution of photoinduced remodeling and that photoswitchable lipids can tune both membrane morphology and phase equilibria, enabling new strategies for stimuli-responsive synthetic cells and soft actuators.

## 1. Introduction

Biological membranes are complex and dynamic assemblies whose physical properties, such as fluidity, thickness, and elasticity, are tightly coupled to cellular function and disease. Their compositional diversity gives rise to lateral heterogeneity and thermodynamic phase behavior, including gel, liquid-ordered (Lo), and liquid-disordered (Ld) phases. Phase separation, driven by differences in lipid chain melting temperatures, represents a fundamental organizational principle of membranes and critically influences protein localization, signaling, and trafficking<sup>1,2</sup>. Through the interplay between lipid packing and membrane mechanics, phase behavior regulates processes ranging from adhesion and division to intracellular transport<sup>3</sup>.

In cellular plasma membranes, this heterogeneity is often conceptualized as lipid rafts, cholesterol- and sphingolipid-enriched domains that serve as platforms for organizing signaling components and facilitating protein-lipid interactions<sup>4-6</sup>. Although lipid heterogeneities in living cells are typically transient and nanoscopic, micron-scale phase separation has been observed in

50 specific organisms such as yeast<sup>7</sup>. To systematically investigate the physical principles underlying  
51 membrane phase coexistence, model systems such as giant unilamellar vesicles (GUVs) provide  
52 a powerful and controllable platform<sup>8,9</sup>. In these systems, phase domains can be directly  
53 visualized by fluorescence microscopy using probes that preferentially partition into specific lipid  
54 environments, for example, enriching in fluid domains while being excluded from gel phases<sup>10</sup>.  
55 Similar to lipids, membrane-associated proteins and peptides exhibit preferential partitioning  
56 depending on their structural and chemical compatibility with local membrane order, thereby  
57 coupling domain organization to functional regulation<sup>4,11,12</sup>.

58 Gel-fluid phase coexistence profoundly alters the mechanical properties of membranes. The  
59 presence of distinct gel and fluid phases drastically affects membrane elasticity<sup>13,14</sup> with ordered  
60 and gel phases generally exhibiting higher bending moduli than disordered ones<sup>15,16</sup>. This  
61 heterogeneity affects not only elasticity but also permeability, as interfaces between coexisting  
62 phases can act as preferential pathways for ion or solute transport<sup>17</sup>. Moreover, the coupling  
63 between in-plane molecular order and topological constraints can drive dramatic morphological  
64 transformations, including shape remodeling and vesicle fission under non-equilibrium  
65 conditions such as thermal gradients<sup>18,19</sup>. These phenomena highlight the central role of phase  
66 behavior in governing membrane architecture and responsiveness.

67 Harnessing phase coexistence in model membranes enables the rational design of systems  
68 with tunable mechanical and transport properties. Phase-separated vesicles have been explored  
69 for controlled drug release, where permeability can be selectively modulated through domain  
70 organization, and for biosensing applications in which changes in domain morphology serve as  
71 responsive readouts<sup>20</sup>. Their integration as functional elements in soft robotics, where  
72 membrane deformations generate directional motion or force<sup>21–23</sup> further illustrates the  
73 potential of membrane phase behavior as an engineering handle. Realizing the full potential of  
74 these systems, however, requires external stimuli capable of dynamically and reversibly  
75 modulating membrane properties with high spatiotemporal precision.

76 Molecular photoswitches provide a powerful strategy for achieving noninvasive, reversible  
77 control over soft matter systems using light<sup>24</sup>. Among these, azobenzene-phosphatidylcholine  
78 (azoPC), a synthetic lipid with an azobenzene moiety within one of the lipid tails (Fig. 1A), has  
79 emerged as a versatile component for synthetic membrane systems and even for applications in  
80 living cells. Upon UV-A (365 nm) irradiation, azoPC undergoes *trans*-to-*cis* isomerization, which  
81 can be reversed with blue light (465 nm), enabling dynamic modulation of membrane properties.  
82 In homogeneous fluid membranes, azoPC photoisomerization has been shown to induce  
83 substantial membrane area increases (up to ~25%) and dramatic softening, reflected in up to an  
84 order-of-magnitude reduction in bending rigidity<sup>25</sup>. It further leads to decreased membrane  
85 thickness and enhanced fluidity<sup>26,27</sup>, and can promote reversible morphological transformations  
86 such as deformation<sup>28</sup>, budding<sup>25</sup>, and endocytosis-like responses<sup>29</sup>. Beyond shape changes,  
87 light-triggered azobenzene isomerization has been linked to altered membrane permeability and  
88 transient pore formation, enabling controlled solute transport<sup>30</sup>. In liquid-liquid (Lo/Ld) phase-  
89 separated ternary lipid mixtures, azoPC has been shown to reversibly reorganize membrane  
90 domains, with UV irradiation converting liquid-ordered regions into liquid-disordered ones<sup>5,31</sup>.  
91 Together, these studies establish azobenzene lipids as precise tools for spatiotemporal control  
92 of membrane structure and function, with demonstrated impact on protein activity<sup>32–34</sup>, and  
93 cellular morphology in living systems<sup>35,36</sup>.

94 Despite this progress, the interplay between photoswitchable lipids and gel-fluid phase  
95 coexistence remains largely unexplored. Gel-fluid systems differ fundamentally from the Lo/Ld  
96 mixtures studied previously: the mechanical contrast between phases is far more pronounced,  
97 with gel domains exhibiting bending moduli orders of magnitude higher than coexisting fluid  
98 regions<sup>16</sup> and line tensions at gel-fluid boundaries are substantially higher<sup>13</sup>. It is therefore  
99 unclear how light-induced conformational changes propagate within such mechanically

100 heterogeneous membranes, and whether the spatial segregation of elastic properties confines  
101 or redirects photoinduced deformation. Here, we introduce azoPC into gel-fluid phase-  
102 separated GUVs to investigate how *trans-cis* isomerization influences domain stability, spatial  
103 confinement of deformation, and membrane remodeling dynamics. By combining controlled  
104 temperature variation with UV and blue light irradiation, we systematically examine how domain  
105 size, organization, and melting behavior modulate the membrane response to light. This  
106 approach allows us to dissect how pre-existing mechanical heterogeneity governs the extent and  
107 localization of photoinduced transformations, revealing new principles for dynamically  
108 controlling complex membrane architectures.

109  
110

## 111 **2. Materials and Methods**

### 112 **2.1 Materials**

113 The lipids 1-stearoyl-2-[(E)-4-(4-((4-butylphenyl)diazenyl)phenyl)butanoyl]-*sn*-glycero-3-  
114 phosphocholine (azoPC), 1-palmitoyl-2-oleoyl-*sn*-glycero-3-phosphocholine (POPC) and 1,2-  
115 dipalmitoyl-*sn*-glycero-3-phosphocholine (DPPC) were purchased from Avanti Polar Lipids  
116 (Alabaster, AL). Glucose, sucrose, and the fluorescent dye 1,2-dioleoyl-*sn*-glycero-3-  
117 phosphoethanolamine labeled with Atto 647N (Atto-647N-DOPE) were purchased from Sigma-  
118 Aldrich (St. Louis, MO, USA). Sulforhodamine B was purchased from Thermo Fischer (Germany).  
119 Chloroform (LiChrosolv<sup>®</sup>) was purchased from Merck KGaA, Germany. Lipids (and 0.1 mol% of  
120 Atto-647N-DOPE) were dissolved in chloroform at typical concentration of 4 mM, and the stock  
121 solutions were stored at -20 °C until use. Sulforhodamine B for membrane leakage was prepared  
122 as a stock concentration 220 μM.

123

### 124 **2.2 Vesicle preparation**

125 The electroformation of GUVs was conducted in an oven at 65°C to ensure the temperature  
126 was above the melting point of the lipids. An aliquot of 12-30 μL of the lipid solution in  
127 chloroform was spread onto two 50 mm × 50 mm indium-tin-oxide (ITO) coated glass slides  
128 (Präzisions Glas & Optik GmbH, Germany). The slides were then clamped together using a 2 mm  
129 Teflon spacer and forming a chamber which was then filled with 100 mM sucrose solution  
130 (resulting in roughly 25 μM lipid in the final GUV solution; note that for calorimetry  
131 measurements, we doubled this concentration to roughly 55 μM to increase the signal-to-noise  
132 ratio). The chamber was placed in the oven for 5 minutes before the application of a sinusoidal  
133 alternating current (AC) field at 10 Hz and 1 V root-mean-square (RMS) for 1.5 hours. Following  
134 electroswelling, the oven was turned off, and the system was allowed to cool gradually to room  
135 temperature over 2 hours. A 0.75 mm Type K Miniature Thermocouple (TC Direct) inserted into  
136 the sample recorded a cooling rate of 0.3 K/min (see Fig. S1 in the Supporting information, SI).

137 Multilamellar vesicles (MLVs) were prepared using the freeze-thaw method following Ref. <sup>37</sup>.  
138 Lipid solutions in chloroform were first dried in a glass vial under a stream of nitrogen, followed  
139 by desiccation for 2 hours. A sucrose solution (100 mM) was warmed up to 65°C and added to  
140 achieve a final lipid concentration of 1 mg/mL, and the mixture was vortexed for 30 seconds.  
141 The sample was then subjected to three cycles of heating in a 65°C water bath, cooling on ice,  
142 and vortexing.

143

### 144 **2.3 Differential scanning calorimetry (DSC)**

145 DSC measurements were performed using a MicroCal VP-DSC system (MicroCal, USA). Both  
146 MLVs and the reference sucrose solution (100 mM) were degassed (ThermoVac, MicroCal, USA)  
147 for 5 minutes before being introduced into the measurement and reference chambers with  
148 volumes of approximately 0.5 mL. The scanning mode was set to a rate of 1 K/min. Data analysis  
149 was conducted using the baseline subtraction functions in Origin 2023 (OriginLab, USA).

150

## 151 **2.4 Microscopy and vesicle contour analysis**

152 GUVs were imaged using an inverted Leica TCS SP8 scanning confocal microscope (Leica,  
153 Germany) equipped with a 63×, 1.2 Numerical Aperture (NA) water immersion HC PL APO CS2  
154 objective, and an HC PL FLUOTAR L 40×, 0.60 NA objective. Atto-647N-DOPE was excited with a  
155 Helium-Neon (HeNe) laser at 633 nm (0.5% laser intensity) and the emission signal was collected  
156 in the range 643–700 nm with photomultiplier detector. Scanning was performed at 600 Hz in  
157 bidirectional mode, with the pinhole size adjusted to 1-4 Airy units (AU), where 1 AU was used  
158 for stacked images used for 3D reconstruction, and larger AUs were employed for observing  
159 irregular deformations.

160 Membrane dynamics were recorded using an inverted Zeiss Axio Observer D1 microscope  
161 (Carl Zeiss, Germany) equipped with a 63×, 1.2 NA water immersion C-Apochromat objective  
162 and a Pco.Edge sCMOS camera (PCO Imaging, Germany), operating at an acquisition rate of 20  
163 frames per second. The observation chamber consisted of two coverslips and a Press-to-Seal  
164 silicone isolator (Invitrogen, Eugene OR, USA) as a spacer. The vesicles were recorded under  
165 bright field.

166 To quantify the degree of GUV deformation, we utilized a contour-tracking algorithm  
167 developed in Ref.<sup>38</sup>. Briefly, the algorithm assigns a set of interpolation points to the GUV  
168 perimeter, where the number of points ( $N$ ) in the contour scales with vesicle size. By monitoring  
169 the coordinates of these points over time, we quantify the degree of shape deviation from a  
170 spherical geometry based on a weighed cumulated relative displacement  $\delta$  of contour points  
171 from their initial coordinates, taken as the onset of UV irradiation, via the expression

$$172 \quad \delta(t) = \frac{\sum_{i=1}^N |\rho_i(t) - R|}{N} \quad (1)$$

173 where  $\rho_i(t)$  is the distance of the  $i$ -th point to the center of the GUV (defined via the averaged  
174 horizontal and vertical coordinates of all points on the contour) at time  $t$  and  $R$  is the initial  
175 average distance of contour points from the center of the vesicle.

176

## 177 **2.5 Light-induced isomerization**

178 Two distinct light-emitting diodes (LED) were utilized to precisely control the isomerization of  
179 azoPC lipids: a high-power UV-LED system and a versatile fiber-coupled LED system.

180 For broad-field UV irradiation, a home-built UV-LED system was employed. This unit  
181 comprised a cooling metal plate and an LED (Star-UV365-01-00-00, Roschwege, Germany) with  
182 a maximum power output of 170 mW. The UV-LED unit was positioned directly onto the sample  
183 observation chamber during experiments to ensure uniform illumination (see Fig. S2a in the SI).

184 For wavelength-specific illumination, a fiber-coupled LED system (Doric, Canada) was used.  
185 This system featured two distinct light sources: a UV LED (365 nm) and a blue LED (450 nm). Light  
186 intensity was controlled via an integrated driver, which offered both manual adjustment via a  
187 control panel and software-based regulation through a connected laptop. The optical fiber  
188 (960  $\mu\text{m}$ , 0.63 NA) from this system was precisely affixed alongside the microscope objective  
189 using a cantilever arm to direct irradiation onto the sample (see SI Fig. S2b). The maximum power  
190 outputs, measured at the sample plane, were determined using a LaserMate 10 sensor and  
191 console (Coherent, USA). The UV light (365 nm) delivered a maximum power of 75 mW, while  
192 the blue light (450 nm) delivered 183 mW.

193

## 194 **2.6 Temperature control**

195 Temperature control of the GUV samples under the microscope was precisely maintained  
196 using a custom-built electrical resistance heater with an observation chamber attached  
197 underneath and mounted on the confocal microscope. The heater consisted of two ITO-coated  
198 glass slides (25 mm  $\times$  50 mm) with adhesive copper tape fixed along their sides. These slides

199 were clamped together with their conductive surfaces facing each other, forming the heating  
200 element, see SI Figs. S3 (also introduced in more detail later in the text and Fig. 4A). To maintain  
201 precise temperature control, the copper tapes were connected to a direct current (DC) generator  
202 (Programmable laboratory power supply unit HCS 3202, Manson, Hong Kong), which was  
203 operated via a laptop and regulated by a custom-developed Proportional–Integral–Derivative  
204 (PID) controller (Multi Control program, in-house developed).

205 Temperature feedback was established using a 0.5 mm diameter Mineral Insulated  
206 Thermocouple (TC Direct, UK), which was directly inserted into the sample chamber. This  
207 thermocouple was connected to a USB-TC01 temperature measurement device (National  
208 Instruments, USA) to provide real-time temperature readings to the PID controller. To prevent  
209 overheating, the maximum current supplied to the heater was limited to 1 A.

210 To maintain thermal stability and prevent heat dissipation through the objective, an objective  
211 heater (Tempcontrol mini, PeCon GmbH, Germany) was attached to the objective and  
212 synchronized with the PID controller for measurements between 30°C and 40°C, while remaining  
213 fixed at 40°C for all sample temperatures exceeding that range.

214 Prior to experiments, the thermocouples were calibrated by immersion in boiling and ice  
215 water. These measurements were cross-referenced against a Pt1000 probe connected to a Testo  
216 735 temperature measuring device (Testo, Germany) to ensure accuracy. For experiments  
217 involving temperature simulations (assessing thermal distribution), calibration measurements  
218 were also performed by attaching thermocouples directly to the coverslip of the observation  
219 chamber and on top of the ITO heater using thermal paste (Peltier contact gel-silver filled,  
220 innovatek, Germany) and heat-resistant tape to minimize heat dissipation and ensure accurate  
221 local temperature readings.

222

## 223 **2.7 Numerical simulations**

224 Numerical simulations were performed using the finite element method software COMSOL  
225 Multiphysics (COMSOL Multiphysics® v. 5.2. [www.comsol.com](http://www.comsol.com). COMSOL AB, Stockholm,  
226 Sweden). The model geometry (Fig. S4) was discretized using triangular elements with refined  
227 boundary layers at fluid interfaces. Heat transfer and fluid flow were solved in a coupled manner:  
228 in the fluid domains (water and air), the heat transfer equation was coupled to the  
229 incompressible Navier-Stokes equations within the Boussinesq approximation to account for  
230 buoyancy-driven convection, while in solid domains (glass, rubber, steel, and ITO) heat  
231 conduction was solved. Dirichlet temperature boundary conditions were imposed at the ITO  
232 interface and on the objective, which were adjusted to match experimentally measured  
233 temperatures at defined probe positions. Full details of the governing equations, boundary  
234 conditions, mesh statistics, and material parameters are provided in the SI (see also Fig. S4 and  
235 Table S1).

236

237

## 238 **3. Results and Discussion**

239 We begin by demonstrating that incorporating azoPC into gel-fluid phase-separated  
240 membranes gives rise to a qualitatively distinct mechanical response to light, manifested as  
241 pronounced crumpling rather than the smooth budding observed in homogeneous fluid vesicles.  
242 We then characterize how this response depends on UV intensity and establish its kinetic  
243 signatures. Finally, we determine the thermotropic phase behavior of the binary azoPC:DPPC  
244 system by calorimetry and temperature-controlled microscopy, providing the thermodynamic  
245 framework needed to interpret the light-driven phenomena described in subsequent sections.

246

### 247 **3.1. Light-induced crumpling in gel-fluid phase-separated vesicles**

248 To investigate how membrane heterogeneity influences photoswitchable deformation, we  
249 incorporated DPPC, a gel-phase lipid with a melting temperature of 41°C<sup>39</sup>, into azoPC-  
250 containing membranes, see Fig. 1A for lipid structures. GUVs were prepared as cell-sized model  
251 membranes<sup>8,9</sup>, enabling direct visualization of phase separation<sup>40</sup> and light-induced  
252 remodeling<sup>25</sup>.

253 We focused on equimolar azoPC:DPPC mixtures to promote extended domain formation and  
254 maximize mechanical contrast between gel and fluid regions. The melting temperature ( $T_m$ ) of  
255 azoPC has not been reported to our knowledge. Although its stearyl-containing tail might  
256 superficially suggest behavior similar to DSPC (1,2-distearoyl-*sn*-glycero-3-phosphocholine,  $T_m$  =  
257 55°C<sup>41</sup>), the presence of a saturated chain alone does not dictate the phase behavior: SOPC (1-  
258 stearyl-2-oleoyl-*sn*-glycero-3-phosphocholine), which also carries a stearyl chain but also one  
259 unsaturated tail, has a  $T_m$  of 6°C<sup>42</sup>. More directly, pure azoPC GUVs display thermal shape  
260 fluctuations and bending rigidities characteristic of fluid membranes at room temperature<sup>25</sup>,  
261 indicating that the  $T_m$  of azoPC lies below 23°C.

262 Binary mixtures of gel- and fluid-phase lipids, such as DPPC:POPC or DPPC:SOPC, are well  
263 known to exhibit gel-fluid phase coexistence at room temperature, typically characterized by  
264 micron-sized gel domains embedded in a fluid matrix depending on composition and thermal  
265 history. By analogy, we expect equimolar DPPC-azoPC membranes at room temperature to  
266 phase-separate into DPPC-rich gel domains and azoPC-rich fluid domains.

267 After electroformation at 60°C, the GUVs were cooled in the oven gradually (~0.3 K/min; Fig.  
268 S1 in the supporting information), occasionally with additional waiting steps at fixed  
269 temperatures, to promote domain coarsening. Slow cooling is known to enhance domain growth  
270 by allowing lipid demixing to approach equilibrium and reducing kinetic trapping of small  
271 domains<sup>43</sup> as we will discuss below. The resulting vesicles were examined by confocal  
272 microscopy.

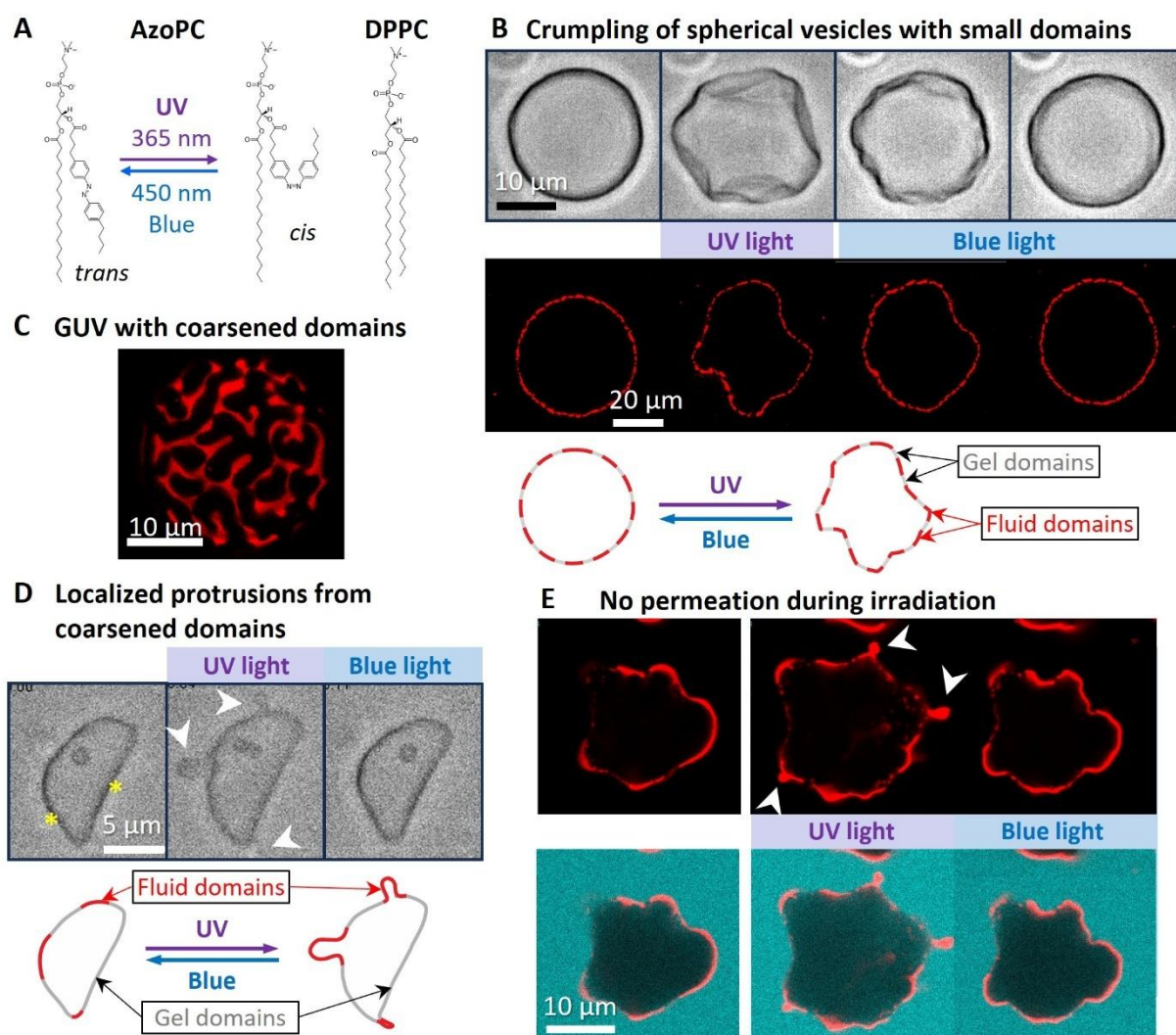
273 Fluorescent labeling with 0.1 mol% Atto-647N-DOPE revealed branched, dye-excluding  
274 domains (Fig. 1B,C), consistent with gel-phase DPPC regions excluding the fluorescent lipid. We  
275 assign the fluorescent regions to azoPC-rich fluid domains and the dark, finger-like regions to  
276 DPPC-rich gel domains. Faster cooling resulted in smaller, more dispersed domains (Fig. 1B,  
277 lower panel), compared to larger, coarsened domains in vesicles where cooling was done slowly  
278 in a stepwise manner (Fig. 1C), confirming the sensitivity of domain size to thermal history.

279 GUVs were irradiated with UV or blue light using a fiber-coupled LED device with precise  
280 intensity control, typically set at 500 mA, corresponding to approximately 75 mW of power at  
281 the sample (Fig. S5). As shown previously<sup>25</sup>, fluid azoPC-doped vesicles exhibit membrane area  
282 expansion stored in transient buds under UV irradiation, yielding a floppy morphology that  
283 reverses under blue light (Fig. S6). Pure DPPC vesicles show no morphological response to UV  
284 light.

285 In marked contrast to fluid azoPC-doped vesicles, equimolar azoPC:DPPC vesicles with  
286 dispersed domains respond to UV light with pronounced crumpling and twisting deformations  
287 (Fig. 1B). Rather than forming large buds leading to homogeneous enlargement, as observed in  
288 homogeneous fluid membranes (Fig. S6), the area expansion appears spatially constrained. The  
289 softer azoPC-rich regions undergo local distortion, while the rigid DPPC-rich domains act as  
290 mechanical scaffolds that resist uniform expansion. The resulting morphology reflects  
291 mechanical frustration between expanding fluid domains and mechanically stiff gel regions (Fig.  
292 1B). Upon blue light irradiation, the vesicles fully recover their initial morphology (Fig. 1B; see  
293 also Movie S1), demonstrating reversible, light-controlled mechanical remodeling in a  
294 heterogeneous membrane.

295 The mechanical response to UV irradiation depends critically on domain size and connectivity,  
296 which in turn are determined by thermal history. In the dispersed-domain regime described

297 above, UV irradiation produces global crumpling distributed across the entire vesicle surface (Fig.  
 298 1B). However, when domains are coarsened by slow passage through the melting transition (as  
 299 discussed below), a qualitatively different response emerges: deformation becomes spatially  
 300 confined to the fluid regions, while the gel domains act as a rigid, unresponsive scaffold (Fig. 1D).  
 301



302  
 303 **Figure 1. Light-induced crumpling and localized budding in phase-separated azoPC:DPPC 1:1 vesicles.**  
 304 (A) Chemical structures of the used lipids. Left: azoPC in its *trans* and *cis* configurations, interconverted by  
 305 UV (365 nm) and blue (here, 460 nm) light; right: DPPC. (B) Light-induced crumpling of GUVs with small  
 306 dispersed domains. Top: Brightfield images of a GUV showing global membrane crumpling upon UV  
 307 irradiation, fully reversed under blue light, see Movie S1. Middle: Confocal cross sections of another GUV  
 308 under UV irradiation illustrating overall deformation: the rigid gel domains resist expansion while fluid  
 309 regions allow local distortion. Bottom: cartoon summarizing the overall crumpling of GUVs with disperse  
 310 small domains. (C) Confocal z-stack projection of a half of a GUV after slow stepwise cooling leading to  
 311 domain coarsening. Dark, branched domains correspond to DPPC-rich gel regions excluding the  
 312 fluorescent dye (0.1 mol% Atto-647N-DOPE), while bright regions are azoPC-rich fluid domains. (D)  
 313 Spatially confined budding in vesicles with coarsened gel domains. Top: Brightfield image sequence of a  
 314 deflated azoPC:DPPC GUV with coarsened domains: flat facets (asterisks) correspond to rigid DPPC-rich gel  
 315 regions that remain practically immobile under UV irradiation (middle), while curved fluid segments  
 316 between them protrude as localized buds (arrowheads). Buds retract fully upon blue light irradiation (right).  
 317 A similar example GUV response is shown in Movie S2. Bottom: cartoons illustrating the localized budding  
 318 response when domains are coarsened contrasting the overall crumpling of vesicles with disperse domains  
 319 as shown in panel B. (E) No permeation during isomerization. Confocal image sequence of a vesicle with  
 320 coarsened domains labeled with 0.1 mol% Atto-647N-DOPE (red) and sulforhodamine B (SRB, cyan) added  
 321 to the external solution (top: membrane channel only, bottom: merged signal). Localized budding of the

322 coarsened fluid domains (arrowheads) is observed under UV irradiation and fully reversed under blue light,  
323 see also Movie S3. The absence of SRB signal inside the vesicle throughout confirms membrane integrity.

324 Coarsened gel domains in deflated vesicles produce characteristic flat facets on the vesicle  
325 surface. These are planar segments whose presence reflects the high stiffness of the membrane  
326 in the gel domains<sup>15</sup>, which resist the curvature that the fluid membrane would otherwise  
327 adopt<sup>14,44</sup>. This faceted morphology is visible in brightfield imaging (Fig. 1D, asterisks).

328 Upon UV irradiation, the faceted regions remain entirely immobile, while the curved fluid  
329 segments between them, which are enriched in azoPC due to the lower bending rigidity of the  
330 fluid phase favoring higher-curvature regions, protrude as localized buds (arrowheads in  
331 Fig. 1D,E, and sketch in D; see also Movies S2 and S3). These buds can protrude outward and  
332 inward imposed by the constant volume constraint. The spatial confinement of the overall  
333 vesicle deformation arises because the gel domains are mechanically inextensible. The excess  
334 area generated by *trans*-to-*cis* photoisomerization is localized predominantly into the fluid  
335 azoPC-rich islands, which store it as outward or inward protrusions.

336 The localized budding is fully reversed upon blue light irradiation, with the vesicle returning  
337 to its pre-irradiation faceted morphology (Fig. 1D,E; Movies S2, S3), confirming that the process  
338 is driven by photoisomerization and not by irreversible membrane remodeling.

339 To verify membrane integrity during this repeated deformation, sulforhodamine B (SRB) was  
340 added to the outer solution (to a final concentration of ~50  $\mu\text{M}$ ) prior to irradiation. No SRB  
341 signal was detected inside the vesicles after more than 10 cycles of UV (5 s each) followed by  
342 blue light (5 s) irradiation, confirming that no membrane leakage occurs during budding (Fig. 1E,  
343 merged channel, Movie S3).

344 Together, the two regimes of (i) global crumpling with dispersed domains (Fig. 1B) and (ii)  
345 localized budding with coarsened domains (Fig. 1D,E) demonstrate that domain size functions  
346 as a structural programmable parameter that determines how photoswitchable area expansion  
347 is distributed across the membrane. Dispersed domains below the percolation threshold allow  
348 global mechanical frustration; coarsened continuous (percolating) domains above it focus  
349 deformation into spatially defined fluid islands. This principle, namely, using gel domain  
350 architecture to direct the localization of light-driven membrane remodeling, offers a strategy for  
351 achieving spatially programmable morphological control in synthetic membrane systems.

352

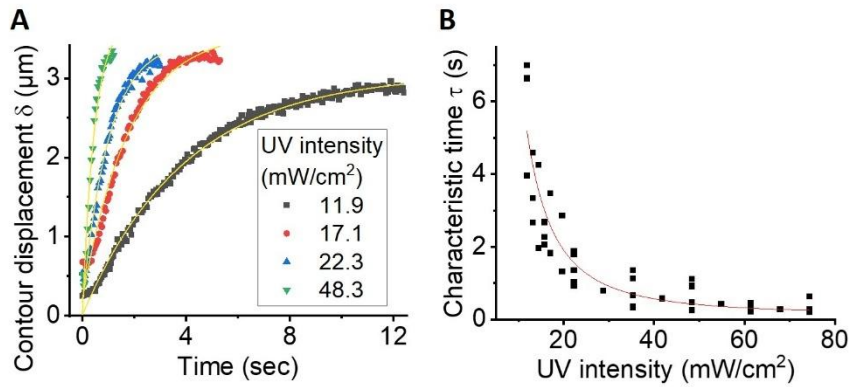
### 353 **3.2. Deformation dynamics depend on UV intensity**

354 To quantify deformation kinetics, we systematically varied UV intensity while remaining well  
355 below previously reported damage thresholds (280–440  $\text{mW}/\text{cm}^2$ ) associated with membrane  
356 defects<sup>45</sup>. Here, intensities ranged from 10 to 75  $\text{mW}/\text{cm}^2$ .

357 The crumpling response in GUVs with small dispersed domains was highly reproducible across  
358 multiple irradiation cycles of the same vesicle, with morphology returning to its original state  
359 after each blue-light exposure (Fig. S7; 13 cycles). The absence of residual deformation suggests  
360 that no irreversible photodamage or photooxidation occurs under our conditions. The fully  
361 reversible shape recovery also indicates that membrane permeability remains unchanged within  
362 experimental resolution; no leakage events were observed during repeated cycling.

363 To quantify shape changes, we tracked vesicle contours using a previously developed  
364 algorithm<sup>38</sup>, which detects the vesicle outline, and computed the average contour displacement  
365 relative to the initial shape (see Eq. 1). This metric captures deformation independently of  
366 direction, overcoming limitations of simple radius or perimeter measurements.

367 Representative time traces for a single vesicle at different UV intensities are shown in Fig. 2A.  
368 The displacement amplitude increases and the response accelerates with increasing UV intensity.  
369 The temporal evolution was fitted with an exponential model,  $\delta(t) = \delta_0 + A_1(1 - e^{-t/\tau})$  from  
370 which a characteristic response time  $\tau$  was extracted for each trial (fits shown in Fig. 2A).



371  
 372 **Figure 2. UV intensity controls deformation kinetics in azoPC-DPPC vesicles (1:1 molar ratio).** (A) Time  
 373 dependence of the relative contour displacement  $\delta$  (defined in Eq. 1) under different UV intensities  
 374 (indicated in the legend) applied to the same GUV. Solid lines (yellow) are single-exponential fits:  $\delta = \delta_0 +$   
 375  $A_1(1 - e^{-t/\tau})$ . The vesicle diameter was  $\sim 30 \mu\text{m}$ . (B) The characteristic response time  $\tau$  as a function of  
 376 UV light intensity plateaus at higher UV intensity, consistent with saturation of the photoisomerization  
 377 process. Data from 4 vesicles. The red curve is an exponential decay fit  $\tau = \tau_\infty + \left(\frac{I_c}{I}\right)^2$  with  $\tau_\infty = 0.12 \text{ s}$   
 378 and  $I_c = 26.7 \text{ mW/cm}^2$  illustrating the saturation behavior.

379 Across vesicles of varying sizes (radius between 15 and 30  $\mu\text{m}$ ),  $\tau$  decreased with increasing  
 380 UV intensity (Fig. 2B). Above approximately 27 mW/cm<sup>2</sup>, the response times approached a  
 381 plateau, suggesting saturation of the photoisomerization process. This behavior is consistent  
 382 with a steady-state balance between *trans*-to-*cis* conversion under UV illumination and  
 383 spontaneous thermal back-isomerization.

384 The scatter in  $\tau$  at fixed intensity likely reflects vesicle-to-vesicle differences in membrane  
 385 tension, since GUV electroformation does not allow precise tension control, as well as variations  
 386 in domain size and connectivity.

387 These results establish UV intensity as a tunable parameter controlling deformation kinetics.  
 388 To understand how the thermotropic phase behavior of the binary system underlies this  
 389 mechanical response, we next characterize its transition temperature.

390

### 391 3.3. Thermotropic behavior of azoPC-DPPC mixtures

392 To determine the phase transition temperature of azoPC-containing membranes, we  
 393 performed differential scanning calorimetry (DSC) on MLV suspensions ( $\sim 1 \text{ mg/mL}$  lipid) and  
 394 compared them to more dilute GUV suspensions at approximately 20-fold lower lipid  
 395 concentration. To increase the signal-to-noise ratio of the GUV measurements, the amount of  
 396 lipid deposited on the ITO-coated glasses during electroformation was doubled relative to the  
 397 preparations used for microscopy observations; note that even at this higher deposition, the  
 398 lower total lipid content of GUV suspensions relative to MLV suspensions results in a low signal-  
 399 to-noise ratio.

400 Pure DPPC samples exhibited a sharp main transition at  $\sim 41^\circ\text{C}$  (Fig. S8), consistent with  
 401 literature values<sup>39</sup>. Pure azoPC membranes exhibited no detectable transition between 20 and  
 402  $60^\circ\text{C}$ , consistent with a fluid state throughout this temperature range.

403 Equimolar azoPC:DPPC mixtures displayed a prominent peak centered at  $31.9^\circ\text{C}$  (Fig. 3),  
 404 superimposed on a broad baseline with a half-width of approximately  $3^\circ\text{C}$ . This curve shape  
 405 indicates partial cooperativity: the sharp peak likely reflects melting of DPPC-rich domains, while  
 406 the broad base is characteristic of extended gel-fluid coexistence in non-ideal binary mixtures<sup>46</sup>.  
 407 The transition temperature of  $31.9^\circ\text{C}$ , which is approximately  $10^\circ\text{C}$  below the  $T_m$  of pure DPPC,  
 408 reflects the fluidizing influence of azoPC on the mixed membrane.

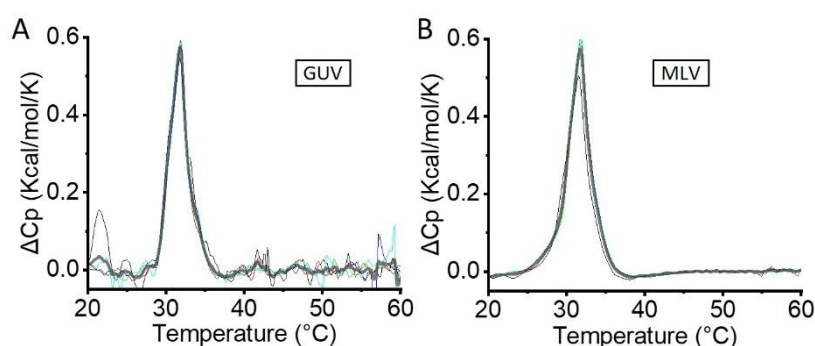
409 We note, however, that the interpretation of the GUV DSC signal warrants caution. The  
 410 increased lipid deposition during electroformation used to improve signal-to-noise may

411 introduce a contribution from non-GUV material, including multilamellar vesicles or lipid  
412 aggregates that did not fully form into unilamellar structures, and we cannot exclude the extent  
413 to which these populations influence the measured profile. For genuinely unilamellar GUV  
414 bilayers, the transition would be expected to be broader than the MLV profile, for two reasons:  
415 First, the higher cooperativity of MLV transitions arises from interlamellar coupling between  
416 stacked bilayers<sup>37</sup>, which is absent in isolated GUVs. Second, the reduced cooperative unit size  
417 and higher effective impurity levels in GUV samples<sup>47</sup> could further broaden the thermotropic  
418 response. Indeed, LAURDAN-based two-photon fluorescence microscopy measurements of the  
419 gel-to-liquid crystalline transition in single-component GUVs revealed a broad transition range  
420 and coexisting membrane regions of distinct generalized polarization over an extended  
421 temperature window<sup>48</sup>. Considering these effects, the true gel-fluid transition in the azoPC:DPPC  
422 GUVs is likely broader than what the DSC curves suggest, with gel-fluid coexistence potentially  
423 detectable more than 10 K above and below the peak transition temperature of 31.9 °C (as  
424 shown previously in LAURDAN-based measurements on GUVs<sup>48</sup>). This is also consistent with the  
425 microscopy observations described in section 3.5, where gel domains persist at sample  
426 temperatures considerably above the calorimetric transition.

427 Interestingly, despite the expectation that interconnected gel domains might form a  
428 mechanically continuous scaffold constraining deformation, microscopy revealed relatively  
429 dispersed dendritic domains even after slow oven cooling (Fig. 1C). Attempts to further increase  
430 domain size by reheating above the transition temperature and re-cooling at the same rate  
431 (0.3 K/min) did not significantly alter domain morphology. This is consistent with domain  
432 connectivity remaining below the percolation threshold required for spatially confined  
433 deformation, and provides a thermodynamic rationale for the global crumpling morphology  
434 observed in Fig. 1B, rather than the localized buckling that would be expected for a fully  
435 percolating gel network. The latter regime, i.e. spatially confined, localized budding, could be  
436 accessed only upon slow passage through the melting transition with prolonged equilibration at  
437 temperatures just above the first microscopic appearance of domains, allowing sufficient time  
438 for domain coarsening and coalescence to build a mechanically continuous gel scaffold.

439 These thermodynamic measurements provide the framework for the temperature-controlled  
440 microscopy experiments described in the following section, in which we directly visualize domain  
441 melting in GUVs and its coupling to light-driven membrane remodeling.

442



443 **Figure 3. Differential scanning calorimetry of 1:1 azoPC:DPPC mixtures.** DSC traces of (A) GUV suspension  
444 (55 μM total lipid; 43 μg/mL) prepared with doubled lipid deposition relative to microscopy samples to  
445 improve signal-to-noise and (B) MLV suspension (1 mg/mL); both samples were prepared in 100 mM  
446 sucrose. Heating rate: 1 K/min. The main transition temperature is ~31.9 °C, approximately 9 °C below the  
447  $T_m$  of pure DPPC (Fig. S8). Note that the GUV profile may contain contributions from non-unilamellar  
448 material and is expected to represent a lower bound on the true breadth of the gel-fluid transition in  
449 isolated GUV bilayers (see main text). Colored curves represent five consecutive heating scans, with the  
450 averaged profile shown as a thick grey line.

452

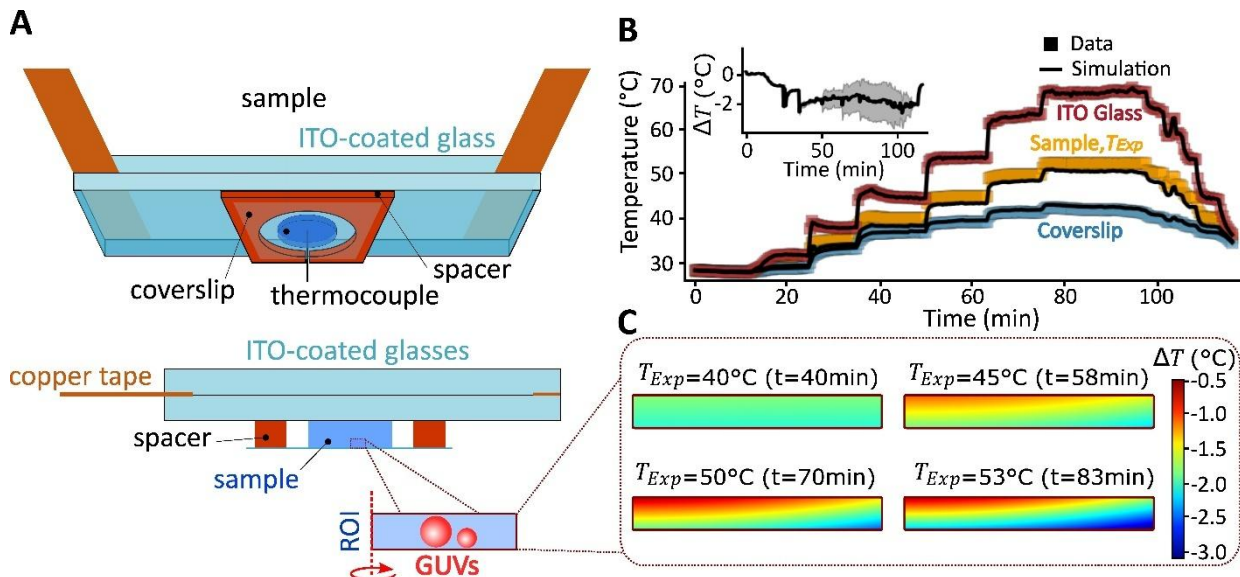
### 3.4. Temperature gradients and numerical calibration of a custom heating chamber for real-time confocal microscopy observations

To observe temperature-dependent domain reorganization, we require a device that maintains optical accessibility for confocal microscopy while heating the sample. We developed a novel custom-made heating device, consisting of ITO glasses and a DC generator, regulated via a PID control program with feedback from the temperature measurements inside the sample. This setup allowed us to maintain optical transparency while heating the samples, enabling real-time imaging under confocal microscopy (Fig. 4A, section 2.6 in the Materials and Methods).

Because heating is applied from above, a vertical temperature gradient develops within the sample, as evidenced by convection currents in the sample that become more pronounced at elevated temperatures. This gradient leads to a systematic deviation between the thermocouple reading and the actual temperature experienced by GUVs resting at the bottom of the chamber (Fig. 4B). This limitation is not unique to our device: in most commercial heating stages, temperature sensors are considerably larger than a vesicle (thus averaging over a larger sample space) and located several hundred microns from the focal plane, while heating is rarely applied homogeneously across the sample.

To estimate the temperature at the GUVs more accurately and assess the magnitude of the temperature gradients, we conducted numerical simulations using thermocouple measurements at two positions: at the ITO glass surface directly above the sample and in the space between the objective and coverslip below the chamber (Fig. 4C, Fig. S4). Throughout this work, we report temperatures as measured by the thermocouple within the sample (hereafter, sample temperature), and accompany each value with the corresponding simulated temperature at the GUV location (hereafter, simulated GUV temperature; note that this represents a range rather than a single value, reflecting the spatial extent of the thermal gradient within the region of interest or ROI), allowing direct comparison across experiments. Our simulations reveal two aspects worth noting at elevated sample temperatures. First, the temperature gradients within the sample are steep enough that a GUV of diameter  $\sim 50 \mu\text{m}$  experiences a temperature difference of roughly  $3^\circ\text{C}$  between its bottom and top (see simulated temperature distribution at a sample temperature of  $50^\circ\text{C}$  in Fig. 4C). Second, the temperature gradients across the whole chamber are substantial, resulting in a difference between the sample thermocouple reading and the simulated GUV temperature: at a sample temperature of  $\sim 50^\circ\text{C}$ , the GUV temperature is up to  $\sim 4^\circ\text{C}$  lower, while at  $\sim 40^\circ\text{C}$  this difference reduces to  $\sim 3^\circ\text{C}$  (see inset in Fig. 4B and Fig. 4C). These gradients are specific to our chamber geometry ( $800 \mu\text{m}$  height, Fig. S9) and are expected to increase further for thicker sample chambers, making instrument-specific calibration particularly important.

Thermal gradients of several Kelvin can be consequential for experiments in which phase transitions spanning only a few degrees are being investigated by microscopy. In the present study, however, these corrections are modest relative to the expected breadth of the gel-fluid transition in azoPC:DPPC GUVs (section 3.3), and do not alter our qualitative conclusions. Importantly, the combination of our custom heating stage with numerical simulations allows us to reliably estimate the actual temperature at the single-GUV level, as we exploit in the following section.

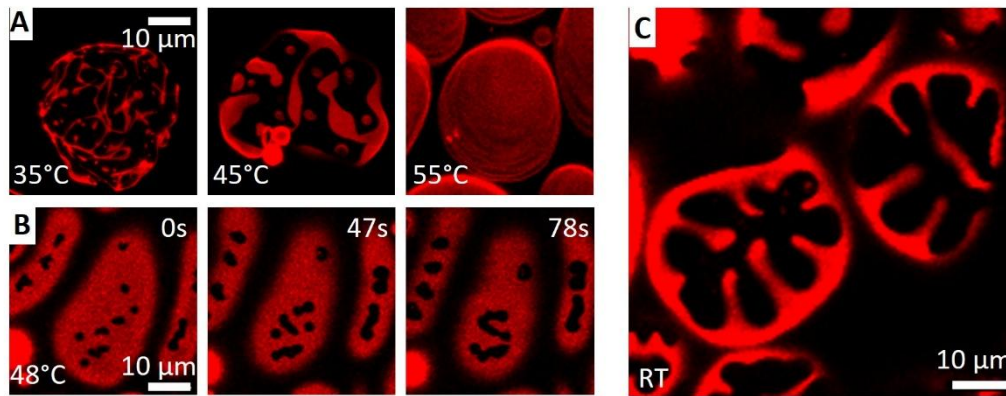


496  
 497 **Figure 4. Temperature distribution in the custom confocal heating chamber and its numerical calibration.**  
 498 (A) Schematic of the temperature-controlled device (see Fig. S9 for drawing with dimensions). Top: 3D  
 499 perspective of the sample and experimental setup. Bottom: 2D cross-section schematically illustrating the  
 500 heating geometry. The region of interest (ROI) where the microscopy measurements and the simulations  
 501 were performed is a cylindrical volume of 0.5 mm radius and 0.05 mm height at the base of the chamber  
 502 (the width of the displayed ROI is not to scale); red spheres schematically represent vesicles of 50 and 20  
 503  $\mu\text{m}$  diameter and the red dashed line represents the axis of rotational symmetry. The two additional  
 504 thermocouples above the ITO glasses and below the sample are not displayed (see Fig. S4 for details). (B)  
 505 Temperatures measured at the top of the device (red), within the sample droplet (orange)  $T_{Exp}(t)$ , and  
 506 below the coverslip (blue), shown as squares (experimental) and black solid curves (numerical simulations),  
 507 as a function of time. The inset shows the difference  $\Delta T(t) = T_{ROI}^{sim}(t) - T_{Exp}(t)$  between the average  
 508 simulated temperature within the ROI,  $T_{ROI}^{sim}$ , and the thermocouple measurement within the sample,  
 509  $T_{Exp}$ ; the shaded region represents the uncertainty based on the maximum and minimum simulated  
 510 temperatures within the ROI. (C) Simulated temperature distribution within the ROI at different  
 511 temperature plateaus in panel B corresponding to the following reading of the thermocouple measuring  
 512 within the sample:  $T_{Exp}(t=40\text{min}) = 40^\circ\text{C}$ ,  $T_{Exp}(t=58\text{min}) = 45^\circ\text{C}$ ,  $T_{Exp}(t=1\text{h}10\text{min}) = 50^\circ\text{C}$  and  
 513  $T_{Exp}(t=1\text{h}23\text{min}) = 53^\circ\text{C}$ . The color scale represents the numerically computed local temperature deviation  
 514  $\Delta T$  from the sample thermocouple reading at each plateau. The simulated temperature ranges,  
 515  $T_{ROI}^{sim}(t=40\text{min}) = 37\div 39^\circ\text{C}$ ,  $T_{ROI}^{sim}(t=58\text{min}) = 42\div 44^\circ\text{C}$ ,  $T_{ROI}^{sim}(t=1\text{h}10\text{min}) = 46\div 50^\circ\text{C}$  and  $T_{ROI}^{sim}(t=1\text{h}23\text{min})$   
 516  $= 49\div 53^\circ\text{C}$ , illustrate how the thermal gradient across the ROI, and hence the overall individual vesicle  
 517 surfaces, evolves with increasing setpoint temperature. Note how the temperature experienced by a GUV  
 518 can differ substantially from the value reported by the sample thermocouple.

519  
 520

### 521 3.5. Temperature-dependent domain reorganization

522 The observations of the vesicles and the detection of domains over time were done using  
 523 confocal microscopy with excitation at 633 nm, which ensures that azoPC remains  
 524 predominantly in its *trans* state during imaging. The GUVs were incrementally heated in steps of  
 525  $5^\circ\text{C}$  and allowed to equilibrate for several minutes before each observation as done in Fig. 4B.  
 526 Even when the sample temperature exceeded the melting transition temperature determined  
 527 by DSC ( $31.9^\circ\text{C}$ ), for example at a sample temperature of  $35^\circ\text{C}$ , the dark gel domains persisted  
 528 for at least 10 minutes, and remained visible even at a sample temperature of  $45^\circ\text{C}$  (Fig. 5A).  
 529 This persistence of gel domains well above the DSC peak transition temperature is consistent  
 530 with the expectation of a very broad gel-fluid transition in GUVs discussed in section 3.3, where  
 531 we argued that coexistence could extend more than 10 K above the calorimetric peak.



532  
 533 **Figure 5. Temperature-dependent melting and domain reorganization in azoPC:DPPC (1:1) GUVs.** (A)  
 534 Domain morphology at successive stages of heating of the same vesicle. Sample temperatures from left to  
 535 right: 35, 45, 55 °C, corresponding to simulated GUV temperature ranges of 32÷34°C, 42÷44°C, and  
 536 51÷55°C respectively (see Fig. 4C for the simulated ROI temperature distribution). Images were acquired  
 537 after ~5 min equilibration at each temperature setpoint. (B) Small, circular gel domains nucleate and their  
 538 boundaries subsequently merge at a fixed sample temperature of 48°C (simulated: 42÷48°C); see Movie  
 539 S4. Time 0 corresponds to the beginning of the recording (roughly after stabilizing the target temperature).  
 540 (C) Large flower-like gel domains observed at the bottom of deflated GUVs at room temperature following  
 541 a controlled heating-cooling cycle in which the sample was first heated until all domains had fully melted,  
 542 then cooled until the first small domains were observed by microscopy, held at that temperature for  
 543 approximately 5 min to allow domain coarsening, and finally allowed to cool passively to room  
 544 temperature. Domain coarsening during the slow cooling step produces the large domains visible here, in  
 545 contrast to the dendritic patterns that reform under faster continuous cooling (Fig. 1B).  
 546

547 In inverted microscope configurations, where heating is applied above the sample while heat  
 548 is lost through the objective and coverslip below, thermocouple measurements systematically  
 549 overestimate the temperature experienced by GUVs resting at the bottom of the chamber. This  
 550 represents a potential source of discrepancy between DSC-determined transition temperatures  
 551 and those inferred from microscopy that, to our knowledge, has not been explicitly quantified  
 552 in the GUV literature. Here, the GUVs only fully melted at sample temperatures well above 50 °C  
 553 (Fig. 5A, last image), which corresponds to 46÷50 °C as assessed by numerical simulation (Fig.  
 554 4B).

555 Starting from fully melted membranes at 55°C sample temperature (51÷55°C simulated) and  
 556 during cooling, small, round gel domains reappeared at a sample temperature of around 48 °C  
 557 (44÷48°C simulated), see Fig. 5B. The appearance of discrete, circular domains is characteristic  
 558 of nucleation and growth below the binodal boundary, where the circular shape minimizes the  
 559 line tension energy of the gel-fluid interface. Over time, the domain boundaries appeared to  
 560 merge while the overall irregular shape of the merged domains was preserved, consistent with  
 561 arrested coarsening at lowered membrane fluidity at decreasing temperature (Fig. 5B; Movie  
 562 S4)<sup>49</sup>. Note that these observations were recorded at the bottom of the vesicle, within a region  
 563 of interest considerably smaller than the full ROI used in the simulations, indicating that the  
 564 actual temperature experienced by the observed GUVs was close to the lower bound of the  
 565 simulated temperature range, namely 44°C.

566 Upon returning to room temperature, the domains further coarsened, with gel domains  
 567 localizing preferentially at the top and bottom of deflated vesicles, forming large flower-like  
 568 patterns (Fig. 5C). This spatial organization reflects the tendency of rigid gel domains to avoid  
 569 regions of high membrane curvature: slightly deflated vesicles adopt an oblate geometry in  
 570 which the equatorial rim is more curved than the top and bottom caps, and the energetic cost  
 571 of bending stiff gel domains drives their redistribution toward the flatter regions. This behavior

572 is consistent with theoretical models treating gel domains as rigid crystalline inclusions  
573 embedded in a fluid membrane<sup>50</sup>.

574 When cooling was performed continuously (rather than stepwise as above allowing for  
575 coarsening time), implying an overall faster cooling rate and no equilibration pauses, finger-like  
576 dendritic patterns reformed (Fig. 1B) instead of the coarsened domains seen in Fig. 5C. The  
577 dendritic morphology is consistent with diffusion-limited domain growth kinetics under rapid  
578 cooling, where the system is unable to equilibrate and domains grow anisotropically along  
579 directions of fastest lipid transport. In equimolar mixtures, this pattern has been associated with  
580 spinodal decomposition<sup>49</sup>, though the distinction from fast nucleation and growth in this  
581 composition range warrants careful interpretation.

582 The microscopy observations confirm that the gel-fluid transition in azoPC:DPPC GUVs is  
583 considerably broader than the DSC profile suggests: domains remained detectable  
584 approximately 18 °C above the DSC peak transition temperature and approximately 13 °C above  
585 the end of the DSC peak baseline (Figs. 3 and 5A), providing direct visual evidence for the  
586 extended coexistence region speculated in section 3.3. Additional contributions from lipid  
587 oxidation or photobleaching during continuous imaging<sup>51</sup> cannot be excluded, though the  
588 independence of the apparent transition temperature on equilibration time argues against  
589 latent heat effects as a primary factor.

590 Additionally, a small fraction of domains failed to melt fully even at sample temperatures of  
591 50°C (46÷50°C simulated), persisting for at least 5 minutes (Fig. S10). This behavior is most  
592 plausibly attributed to two factors. First, large, compact gel domains have a lower perimeter-to-  
593 area ratio than smaller ones, meaning that lipid exchange between the gel domain and the  
594 surrounding fluid phase is kinetically slower and the domain interior is effectively shielded from  
595 the phase boundary and dissolves on a longer timescale even when thermodynamically unstable  
596 above  $T_m$ . Indeed, the size dependence of melting kinetics has a straightforward physical  
597 analogy: just as an iceberg melts more slowly than a snowball of the same composition due to  
598 its smaller surface-to-volume ratio, several-microns-large gel domains in GUVs dissolve more  
599 slowly than sub-microscopic (nanometric) domains in MLVs and LUVs. This could be why, at  
600 similar heating/cooling rates, bulk calorimetric measurements on those smaller assemblies  
601 report a sharper transition than direct microscopy of GUVs. This kinetic trapping of large  
602 domains upon heating is the mirror image of the arrested coarsening observed upon cooling  
603 discussed above. Second, trace impurities in the lipid preparations are known to stabilize gel  
604 domains anomalously, as demonstrated for DPPC GUVs where glucose-derived contaminants  
605 produced dye-depleted domains persisting well above the main transition temperature<sup>47</sup>. The  
606 combination of these two effects, namely slow dissolution kinetics of large domains and  
607 impurity-mediated stabilization, provides a sufficient explanation for the residual domains  
608 observed here, without invoking an intrinsic elevation of the transition temperature of the lipid  
609 mixture itself.

610 We also explored the use of LAURDAN as an environmentally sensitive fluorescent reporter  
611 of the gel-fluid transition, following its established application in GUV imaging<sup>48</sup>. In that study,  
612 LAURDAN two-photon microscopy was used to image coexisting gel and fluid domains in binary  
613 DPPC-containing GUVs. This binary system with transition temperatures in the range 15–41 °C  
614 depending on composition is directly comparable to our system. LAURDAN reports the gel-fluid  
615 transition through a red shift in its emission spectrum upon moving from gel to fluid  
616 environments, providing a spatially resolved readout of membrane order. However, LAURDAN  
617 turned out not to be suitable as a phase indicator in azoPC:DPPC membranes due to the overlap  
618 of its excitation-emission spectrum with the photoisomerization spectrum of azoPC, which gives  
619 rise to Förster resonance energy transfer (FRET) between the two molecules. As a consequence,  
620 when LAURDAN was present at 0.5 mol% in azoPC-containing GUVs at room temperature, the

621 vesicles exhibited no detectable fluorescence and no detectable respond to UV or blue light  
622 irradiation in terms of morphology changes (Fig. S11).

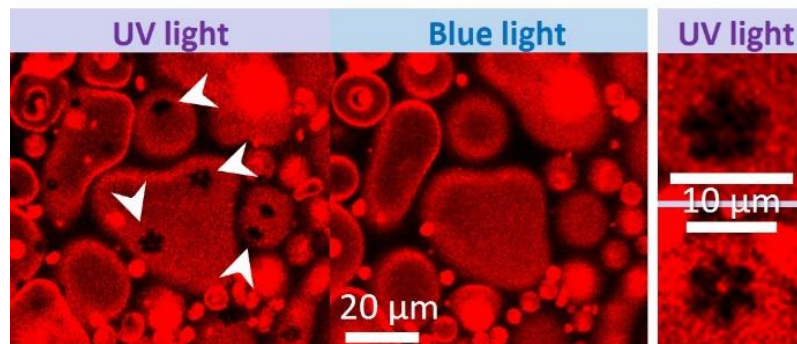
623 We should note that, potential tension-induced shifts in the observations in this section can  
624 be ignored as the vesicles were deflated. Micropipette aspiration experiments have  
625 demonstrated that increasing membrane tension decreases the miscibility transition  
626 temperature in systems of liquid-ordered/liquid-disordered phase coexistence, with a tension  
627 increase of  $\sim 0.1$  mN/m producing a shift of several tenths of a Kelvin<sup>52</sup>. While that study  
628 addressed liquid-liquid coexistence specifically, the same thermodynamic argument is expected  
629 to apply to gel-fluid phase boundaries<sup>53</sup>, and we therefore emphasize the precaution of working  
630 with deflated vesicles.

631

### 632 3.6. Photoinduced domain nucleation in fully melted azoPC:DPPC membranes

633 At temperatures where gel domains have fully melted and the membrane is homogeneous,  
634 we exposed the vesicles to UV light. In homogeneous fluid azoPC membranes, UV irradiation is  
635 known to produce membrane area expansion stored in transient buds<sup>25</sup> (see also Fig. S6a), and  
636 similar area expansion was observed in fully melted azoPC:DPPC vesicles at a sample  
637 temperature of 55°C (51÷55°C simulated). In addition, however, we observed an unexpected  
638 phenomenon: small ( $\sim 3$ -6  $\mu\text{m}$ ) flower-like, six-lobed dye-excluding domains appeared under UV  
639 irradiation, a process fully reversed under blue light (Fig. 6; Movie S5). The reversibility under  
640 blue light confirms that domain formation is a direct consequence of photoisomerization and  
641 not of UV-induced chemical modification or photooxidation of the membrane.

642



643

644 **Figure 6. Photoinduced flower-like gel domain formation in fully melted azoPC:DPPC GUVs.**  
645 Confocal images showing the membrane before UV irradiation (left, homogeneous fluorescence  
646 indicating a fully mixed fluid membrane), under UV irradiation (middle, small six-lobed dye-  
647 excluding domains indicated by arrowheads), and after blue light exposure (right, full recovery of  
648 the homogeneous state); see Movie S5. The flower-like domains, approximately 3-6  $\mu\text{m}$  in size,  
649 appear within  $\sim 5$ s of UV irradiation at  $\sim 74$ mW/cm<sup>2</sup> and dissolve fully upon blue light irradiation,  
650 confirming their photoisomerization origin. Images were acquired at 55 °C (51÷55 °C simulated).

651

652 The unexpected appearance of gel-like domains in a membrane that is fully melted well above  
653 the bulk  $T_m$  of the mixture is puzzling. We considered several candidate mechanisms in turn,  
654 noting the deficiencies of each before arriving at the most plausible interpretation.

655 A first hypothesis is that *cis*-azoPC molecules self-associate via  $\pi$ - $\pi$  stacking of their  
656 azobenzene moieties, locally clustering in a way that excludes the fluorescent dye and mimics a  
657 gel-like environment. However, *trans*-to-*cis* isomerization in pure azoPC supported bilayers has  
658 been shown to increase lipid diffusivity approximately twofold<sup>45,54</sup>, demonstrating that the *cis*  
659 state produces a more fluid, not less fluid, membrane environment. Self-association of azoPC  
660 into a gel-like phase is therefore inconsistent with measured molecular mobility data.

661 A second hypothesis could be related to potential, uncontrollable leaflet compositional  
662 asymmetry: if azoPC is enriched in one leaflet relative to the other, UV irradiation would

663 generate differential area expansion between the two leaflets, imposing a differential stress that  
664 has been shown both experimentally and theoretically to nucleate gel domains in otherwise fluid  
665 membranes<sup>55,56</sup>. While this mechanism is physically well-grounded, it is unlikely to be relevant  
666 here: electroformation is well established to produce symmetric PC bilayers, and there is no a  
667 priori reason to expect preferential partitioning of azoPC to one leaflet during vesicle  
668 preparation. Furthermore, upon UV irradiation, potential leaflet asymmetry would have resulted  
669 in large spontaneous curvature as leaflet area difference is enhanced by the asymmetric  
670 distribution of azoPC triggering tube formation, which we do not observe.

671 A third hypothesis, and in our view the most physically compelling, is that photoisomerization  
672 effectively shifts the phase diagram of the azoPC:DPPC mixture to higher temperatures. In  
673 particular, we speculate that the *trans* and *cis* isomers of azoPC have different transition  
674 temperatures when mixed with DPPC. While our DSC measurements established a transition  
675 temperature of 31.9°C for the *trans*-azoPC:DPPC system (Fig. 3), the geometric incompatibility  
676 between the kinked *cis* tail and the straight acyl chains of DPPC (Fig. 1A) may raise this transition  
677 temperature substantially upon UV irradiation. The severely kinked tail of *cis*-azoPC makes it a  
678 far poorer co-solvent for DPPC in the fluid phase, reducing the free energy of mixing and  
679 effectively shifting  $T_m$  of the mixture upward. If this upward shift is sufficient to bring the  
680 effective  $T_m$  of the *cis*-azoPC:DPPC system above the actual temperature at the GUVs, DPPC-rich  
681 gel domains will nucleate spontaneously in the newly supersaturated membrane.

682 This hypothesis accounts naturally for all key observations. It explains why the domains are  
683 dye-excluding DPPC-rich gel domains: DPPC is expelled from the *cis*-azoPC-rich fluid phase as its  
684 solubility in it decreases. It explains the contrast with cholesterol-containing liquid-  
685 ordered/liquid-disordered systems, where UV light suppresses rather than induces phase  
686 separation<sup>31</sup>: in those systems the relevant comparison is between *cis*-azoPC and cholesterol as  
687 ordering agents, not between *cis* and *trans* as co-solvents for a gel-forming lipid, and the absence  
688 of cholesterol in our system is therefore the critical compositional difference. Finally, it explains  
689 the complete reversibility under blue light: isomerization to *trans*-azoPC recovers the more  
690 favorable mixing geometry, lowering the effective  $T_m$  and dissolving the domains. A direct  
691 experimental test of this hypothesis would be a DSC measurement on *cis*-azoPC:DPPC  
692 multilamellar vesicles, which would be predicted to exhibit a higher transition temperature than  
693 the *trans* system characterized in Fig. 3. However, such an experiment is technically challenging  
694 (if not unfeasible) due to the spontaneous thermal relaxation of *cis*-azoPC.

695 The six-lobed morphology of the photoinduced domains, reminiscent of the flower-shaped  
696 2D crystalline domains reported by Wan et al. in DPPC:DOPC GUVs<sup>50</sup>, is consistent with the  
697 tendency of such rigid domains embedded in a fluid membrane to adopt developable shapes to  
698 minimize strain<sup>50</sup> (developable shapes are those that can bend along one direction while  
699 remaining flat along another, like the petals of a flower wrapping around a sphere, thereby  
700 avoiding the large elastic strain that would arise from bending simultaneously in two directions).  
701 In Wan et al., the petal instability is driven by elevated membrane tension building up during  
702 cooling on large vesicles. However, in our system tension is reduced by UV irradiation, so the  
703 petal morphology likely reflects the intrinsic preference of a DPPC-rich crystalline domain for  
704 developable shapes, rather than a tension-driven instability.

705 Regardless of the precise mechanism, the reversible light-controlled nucleation and  
706 dissolution of gel domains in a fluid membrane represents a qualitatively distinct phenomenon  
707 from the crumpling and mechanical frustration described in earlier sections (Fig. 1), and one that  
708 highlights the richness of photoswitchable binary membranes beyond simple area-expansion  
709 effects.

710

#### 711 4. Conclusions

712 We demonstrated that photoswitchable lipids provide a versatile handle for dynamically  
713 controlling the mechanical response of gel-fluid phase-separated model membranes, with the  
714 nature of the response determined by the spatial organization of the coexisting phases.

715 In azoPC:DPPC (1:1) GUVs at room temperature, UV-induced *trans*-to-*cis* isomerization  
716 generates excess membrane area that is stored as mechanical deformation. The character of this  
717 deformation depends critically on the size and connectivity of the gel domains (Fig. 1), which is  
718 in turn set by the thermal history of the sample. When gel domains are small and dispersed (as  
719 in vesicles cooled rapidly through the melting transition) the area expansion generates global  
720 crumpling distributed across the entire vesicle, reflecting mechanical frustration between  
721 expanding fluid regions and a non-percolating gel scaffold. When gel domains are coarsened by  
722 slow stepwise cooling (producing a mechanically percolating network) deformation is spatially  
723 confined: flat gel facets remain immobile while the fluid azoPC-rich islands between them  
724 protrude as localized, reversible buds. In both regimes the deformation is fully reversed by blue  
725 light irradiation, confirming that the response is driven by photoisomerization rather than  
726 chemical modification. Membrane integrity is preserved throughout, as verified by the absence  
727 of leakage of an encapsulated fluorescent dye (Fig. 1E).

728 Calorimetric measurements on azoPC:DPPC MLV and GUV suspensions establish a gel-fluid  
729 transition temperature of 31.9°C for the *trans* system (approximately 10°C below the  $T_m$  of pure  
730 DPPC, Figs. 3, S8) and temperature-controlled confocal microscopy directly visualizes domain  
731 melting and re-nucleation (Fig. 5). Direct microscopy observations confirm that the transition in  
732 GUVs is far broader than the calorimetric profile suggests, with gel domains persisting well above  
733 the DSC peak, a finding we attribute to the reduced interlamellar cooperativity and larger  
734 domain size in GUVs compared to MLVs. A custom-built heating stage with numerical  
735 temperature calibration revealed that thermocouple-based measurements in inverted  
736 microscope configurations systematically overestimate the temperature at the GUV location due  
737 to vertical thermal gradients (Fig. 4), a source of systematic error in temperature-resolved GUV  
738 experiments that has not previously been explicitly quantified.

739 Perhaps the most unexpected finding is the light-induced nucleation of gel domains in fully  
740 melted, homogeneous membranes held well above the bulk transition temperature of the *trans*  
741 mixture (Fig. 6). We propose that this phenomenon arises because *trans*-to-*cis*  
742 photoisomerization raises the effective gel-fluid transition temperature of the binary mixture:  
743 the kinked *cis* tail of azoPC is geometrically incompatible with the straight acyl chains of DPPC,  
744 reducing their mutual miscibility in the fluid phase and driving DPPC-rich gel domains to nucleate.  
745 This represents a photoswitchable, fully reversible shift in membrane phase behavior. This  
746 finding is a fundamentally different phenomenon from the area-expansion-driven deformation  
747 described in prior work on homogeneous azoPC membranes and on Lo/Ld phase-separated  
748 systems containing cholesterol<sup>31</sup>. The small flower-like morphology of the photoinduced  
749 domains, with six-fold symmetry consistent with the crystalline packing of DPPC, reflects the  
750 tendency of rigid gel inclusions to adopt shapes that minimize elastic strain in the surrounding  
751 fluid membrane.

752 These findings establish several principles with broad relevance. First, gel domain  
753 architecture controlled through thermal history functions as a structural parameter that  
754 programs the spatial distribution of light-driven membrane remodeling, from globally  
755 distributed to locally confined. Second, photoswitchable lipids can modulate not only membrane  
756 mechanics but also phase equilibria, enabling reversible, light-controlled switching between  
757 mixed and phase-separated states without changing composition or temperature. Third, the  
758 temperature calibration methodology developed here is of general value for any quantitative  
759 GUV experiment involving a heating stage on an inverted microscope.

760 Looking ahead, the ability to reversibly and non-invasively switch between global and local  
761 membrane deformation modes using light opens possibilities for the design of stimuli-  
762 responsive synthetic cells (see e.g. Ref. <sup>57</sup>), membrane-based actuators in soft robotics<sup>58</sup>, and  
763 compartmentalized reaction systems where domain boundaries serve as programmable sites for  
764 local morphological change.

765  
766

#### 767 **Author contributions**

768 R.D. supervised the project. All authors designed the experiments, T.-W.S. performed the  
769 experiments and analyzed the data. M.A. assisted with establishing the irradiation and  
770 observation protocols. E.S. performed the numerical simulations. T.-W.S., E.S. and R.D. wrote  
771 the manuscript. All authors edited the manuscript.

772

#### 773 **Notes**

774 The authors declare no conflict of interest

775

#### 776 **Funding sources**

777 This work was supported by Germany's Excellence Strategy, EXC 2008/1 (UniSysCat), Grant  
778 390540038.

779

#### 780 **Acknowledgements**

781 TWS acknowledges the support of Klaus Bienert for developing the heating device control  
782 software and setup.

783

#### 784 **Data availability**

785 The data supporting this article have been included as part of the Supplementary Information.

#### 786 **References**

- 787 (1) Elson, E. L.; Fried, E.; Dolbow, J. E.; Genin, G. M. Phase Separation in Biological  
788 Membranes: Integration of Theory and Experiment. *Annu. Rev. Biophys.* **2010**, *39* (1),  
789 207–226. <https://doi.org/10.1146/annurev.biophys.093008.131238>.
- 790 (2) Simons, K.; Sampaio, J. L. Membrane Organization and Lipid Rafts. *Cold Spring Harbor*  
791 *Perspectives in Biology* **2011**, *3* (10), a004697–a004697.  
792 <https://doi.org/10.1101/cshperspect.a004697>.
- 793 (3) Van Meer, G.; Voelker, D. R.; Feigenson, G. W. Membrane Lipids: Where They Are and  
794 How They Behave. *Nat Rev Mol Cell Biol* **2008**, *9* (2), 112–124.  
795 <https://doi.org/10.1038/nrm2330>.
- 796 (4) Sezgin, E.; Levental, I.; Mayor, S.; Eggeling, C. The Mystery of Membrane Organization:  
797 Composition, Regulation and Roles of Lipid Rafts. *Nat Rev Mol Cell Biol* **2017**, *18* (6), 361–  
798 374. <https://doi.org/10.1038/nrm.2017.16>.
- 799 (5) Hartrampf, N.; Leitao, S. M.; Winter, N.; Toombs-Ruane, H.; Frank, J. A.; Schwille, P.;  
800 Trauner, D.; Franquelim, H. G. Structural Diversity of Photoswitchable Sphingolipids for  
801 Optodynamic Control of Lipid Microdomains. *Biophysical Journal* **2023**,  
802 S0006349523001352. <https://doi.org/10.1016/j.bpj.2023.02.029>.
- 803 (6) Simons, K.; Ikonen, E. Functional Rafts in Cell Membranes. *Nature* **1997**, *387* (6633), 569–  
804 572. <https://doi.org/10.1038/42408>.
- 805 (7) Leveille, C. L.; Cornell, C. E.; Merz, A. J.; Keller, S. L. Yeast Cells Actively Tune Their  
806 Membranes to Phase Separate at Temperatures That Scale with Growth Temperatures.

- 807 *Proc. Natl. Acad. Sci. U.S.A.* **2022**, *119* (4), e2116007119.  
808 <https://doi.org/10.1073/pnas.2116007119>.
- 809 (8) *The Giant Vesicle Book*, 1st ed.; Dimova, R., Marques, C. M., Eds.; CRC Press: Boca Raton,  
810 FL : CRC Press, Taylor & Francis Group, [2020], 2019.  
811 <https://doi.org/10.1201/9781315152516>.
- 812 (9) Dimova, R. Giant Vesicles and Their Use in Assays for Assessing Membrane Phase State,  
813 Curvature, Mechanics, and Electrical Properties. *Annu. Rev. Biophys.* **2019**, *48* (1), 93–119.  
814 <https://doi.org/10.1146/annurev-biophys-052118-115342>.
- 815 (10) Veatch, S. L.; Keller, S. L. Miscibility Phase Diagrams of Giant Vesicles Containing  
816 Sphingomyelin. *Phys. Rev. Lett.* **2005**, *94* (14), 148101.  
817 <https://doi.org/10.1103/PhysRevLett.94.148101>.
- 818 (11) Pike, L. J. Lipid Rafts: Bringing Order to Chaos. *Journal of Lipid Research* **2003**, *44* (4), 655–  
819 667. <https://doi.org/10.1194/jlr.R200021-JLR200>.
- 820 (12) Patarraia, S.; Liu, Y.; Lipowsky, R.; Dimova, R. Effect of Cytochrome c on the Phase Behavior  
821 of Charged Multicomponent Lipid Membranes. *Biochimica et Biophysica Acta (BBA) -*  
822 *Biomembranes* **2014**, *1838* (8), 2036–2045.  
823 <https://doi.org/10.1016/j.bbamem.2014.04.019>.
- 824 (13) Baumgart, T.; Das, S.; Webb, W. W.; Jenkins, J. T. Membrane Elasticity in Giant Vesicles  
825 with Fluid Phase Coexistence. *Biophysical Journal* **2005**, *89* (2), 1067–1080.  
826 <https://doi.org/10.1529/biophysj.104.049692>.
- 827 (14) Lipowsky, R.; Dimova, R. Domains in Membranes and Vesicles. *J. Phys.: Condens. Matter*  
828 **2002**, *15* (1), S31. <https://doi.org/10.1088/0953-8984/15/1/304>.
- 829 (15) Dimova, R.; Pouligny, B.; Dietrich, C. Pretransitional Effects in  
830 Dimyristoylphosphatidylcholine Vesicle Membranes: Optical Dynamometry Study.  
831 *Biophysical Journal* **2000**, *79* (1), 340–356. [https://doi.org/10.1016/S0006-](https://doi.org/10.1016/S0006-3495(00)76296-5)  
832 [3495\(00\)76296-5](https://doi.org/10.1016/S0006-3495(00)76296-5).
- 833 (16) Dimova, R. Recent Developments in the Field of Bending Rigidity Measurements on  
834 Membranes. *Advances in Colloid and Interface Science* **2014**, *208*, 225–234.  
835 <https://doi.org/10.1016/j.cis.2014.03.003>.
- 836 (17) Cordeiro, R. M. Molecular Structure and Permeability at the Interface between Phase-  
837 Separated Membrane Domains. *J. Phys. Chem. B* **2018**, *122* (27), 6954–6965.  
838 <https://doi.org/10.1021/acs.jpcc.8b03406>.
- 839 (18) Hirst, L. S.; Ossowski, A.; Fraser, M.; Geng, J.; Selinger, J. V.; Selinger, R. L. B. Morphology  
840 Transition in Lipid Vesicles Due to In-Plane Order and Topological Defects. *Proceedings of*  
841 *the National Academy of Sciences* **2013**, *110* (9), 3242–3247.  
842 <https://doi.org/10.1073/pnas.1213994110>.
- 843 (19) Kudella, P. W.; Preißinger, K.; Morasch, M.; Dirscherl, C. F.; Braun, D.; Wixforth, A.;  
844 Westerhausen, C. Fission of Lipid-Vesicles by Membrane Phase Transitions in Thermal  
845 Convection. *Sci Rep* **2019**, *9* (1), 18808. <https://doi.org/10.1038/s41598-019-55110-0>.
- 846 (20) Nikoleli, G.-P.; Siontorou, C. G.; Nikolelis, M.-T.; Bratakou, S.; Bendos, D. K. Recent Lipid  
847 Membrane-Based Biosensing Platforms. *Applied Sciences* **2019**, *9* (9), 1745.  
848 <https://doi.org/10.3390/app9091745>.
- 849 (21) Shoji, K.; Kawano, R. Recent Advances in Liposome-Based Molecular Robots.  
850 *Micromachines* **2020**, *11* (9), 1–20. <https://doi.org/10.3390/M11090788>.
- 851 (22) Razavi, S.; Wong, F.; Abubaker-Sharif, B.; Matsubayashi, H. T.; Nakamura, H.; Nguyen, N.  
852 T. H.; Robinson, D. N.; Chen, B.; Iglesias, P. A.; Inoue, T. Synthetic Control of Actin  
853 Polymerization and Symmetry Breaking in Active Protocells. *Sci. Adv.* **2024**, *10* (24),  
854 eadk9731. <https://doi.org/10.1126/sciadv.adk9731>.

- 855 (23) Tanaka, S.; Takiguchi, K.; Hayashi, M. Repetitive Stretching of Giant Liposomes Utilizing  
856 the Nematic Alignment of Confined Actin. *Commun Phys* **2018**, *1* (1), 18.  
857 <https://doi.org/10.1038/s42005-018-0019-2>.
- 858 (24) Boelke, J.; Hecht, S. Designing Molecular Photoswitches for Soft Materials Applications.  
859 *Advanced Optical Materials* **2019**, *7* (16), 1900404.  
860 <https://doi.org/10.1002/adom.201900404>.
- 861 (25) Aleksanyan, M.; Grafmüller, A.; Crea, F.; Georgiev, V. N.; Yandrapalli, N.; Block, S.;  
862 Heberle, J.; Dimova, R. Photomanipulation of Minimal Synthetic Cells: Area Increase,  
863 Softening, and Interleaflet Coupling of Membrane Models Doped with Azobenzene-Lipid  
864 Photoswitches. *Advanced Science* **2023**, *10* (31), 2304336.  
865 <https://doi.org/10.1002/advs.202304336>.
- 866 (26) Socrier, L.; Steinem, C. Cover Feature: Photo-Lipids: Light-Sensitive Nano-Switches to  
867 Control Membrane Properties (ChemPlusChem 11/2023). *ChemPlusChem* **2023**, *88* (11),  
868 e202300440. <https://doi.org/10.1002/cplu.202300440>.
- 869 (27) Manafirad, A.; Menendez, C. A.; Perez-Lemus, G. R.; Thayumanavan, S.; de Pablo, J. J.;  
870 Dinsmore, A. D. Structural and Mechanical Response of Two-Component Photoswitchable  
871 Lipid Bilayer Vesicles. *Langmuir* **2023**, *39* (45), 15932–15941.  
872 <https://doi.org/10.1021/acs.langmuir.3c01764>.
- 873 (28) Pernpeintner, C.; Frank, J. A.; Urban, P.; Roeske, C. R.; Pritzl, S. D.; Trauner, D.; Lohmüller,  
874 T. Light-Controlled Membrane Mechanics and Shape Transitions of Photoswitchable Lipid  
875 Vesicles. *Langmuir* **2017**, *33* (16), 4083–4089.  
876 <https://doi.org/10.1021/acs.langmuir.7b01020>.
- 877 (29) Mangiarotti, A.; Aleksanyan, M.; Siri, M.; Sun, T.-W.; Lipowsky, R.; Dimova, R.  
878 Photoswitchable Endocytosis of Biomolecular Condensates in Giant Vesicles. *Advanced*  
879 *Science* **2024**, *11* (23), 2309864. <https://doi.org/10.1002/advs.202309864>.
- 880 (30) Albanese, P.; Cataldini, S.; Ren, C. Z.-J.; Valletti, N.; Brunetti, J.; Chen, J. L.-Y.; Rossi, F.  
881 Light-Switchable Membrane Permeability in Giant Unilamellar Vesicles. *Pharmaceutics*  
882 **2022**, *14* (12), 2777. <https://doi.org/10.3390/pharmaceutics14122777>.
- 883 (31) Urban, P.; Pritzl, S. D.; Konrad, D. B.; Frank, J. A.; Pernpeintner, C.; Roeske, C. R.; Trauner,  
884 D.; Lohmüller, T. Light-Controlled Lipid Interaction and Membrane Organization in  
885 Photolipid Bilayer Vesicles. *Langmuir* **2018**, *34* (44), 13368–13374.  
886 <https://doi.org/10.1021/acs.langmuir.8b03241>.
- 887 (32) Crea, F.; Vorkas, A.; Redlich, A.; Cruz, R.; Shi, C.; Trauner, D.; Lange, A.; Schlesinger, R.;  
888 Heberle, J. Photoactivation of a Mechanosensitive Channel. *Front. Mol. Biosci.* **2022**, *9*,  
889 905306. <https://doi.org/10.3389/fmolb.2022.905306>.
- 890 (33) Doroudgar, M.; Morstein, J.; Becker-Baldus, J.; Trauner, D.; Glaubitz, C. How  
891 Photoswitchable Lipids Affect the Order and Dynamics of Lipid Bilayers and Embedded  
892 Proteins. *J. Am. Chem. Soc.* **2021**, *143* (25), 9515–9528.  
893 <https://doi.org/10.1021/jacs.1c03524>.
- 894 (34) Erkan-Candag, H.; Krivic, D.; Gsell, M. A. F.; Aleksanyan, M.; Stockner, T.; Dimova, R.;  
895 Tiapko, O.; Groschner, K. Characterization of DAG Binding to TRPC Channels by Target-  
896 Dependent Cis–Trans Isomerization of OptoDARg. *Biomolecules* **2022**, *12* (6), 799.  
897 <https://doi.org/10.3390/biom12060799>.
- 898 (35) Jiménez-Rojo, N.; Feng, S.; Morstein, J.; Pritzl, S. D.; Asaro, A.; López, S.; Xu, Y.; Harayama,  
899 T.; Vepřek, N. A.; Arp, C. J.; Reynders, M.; Novak, A. J. E.; Kanshin, E.; Lipfert, J.;  
900 Ueberheide, B.; Muñoz, M.; Lohmüller, T.; Riezman, H.; Trauner, D. Optical Control of  
901 Membrane Viscosity Modulates ER-to-Golgi Trafficking. *ACS Cent. Sci.* **2025**, *11* (9), 1736–  
902 1752. <https://doi.org/10.1021/acscentsci.5c00606>.
- 903 (36) Höglspurger, F.; Vos, B. E.; Hofemeier, A. D.; Seyfried, M. D.; Stövesand, B.; Alavizargar, A.;  
904 Topp, L.; Heuer, A.; Betz, T.; Ravoo, B. J. Rapid and Reversible Optical Switching of Cell

- 905 Membrane Area by an Amphiphilic Azobenzene. *Nat Commun* **2023**, *14* (1), 3760.  
 906 <https://doi.org/10.1038/s41467-023-39032-0>.
- 907 (37) Kreuzberger, M. A.; Tejada, E.; Wang, Y.; Almeida, P. F. GUVs Melt Like LUVs: The Large  
 908 Heat Capacity of MLVs Is Not Due to Large Size or Small Curvature. *Biophysical Journal*  
 909 **2015**, *108* (11), 2619–2622. <https://doi.org/10.1016/j.bpj.2015.04.034>.
- 910 (38) Gracià, R. S.; Bezlyepkina, N.; Knorr, R. L.; Lipowsky, R.; Dimova, R. Effect of Cholesterol on  
 911 the Rigidity of Saturated and Unsaturated Membranes: Fluctuation and  
 912 Electrodeformation Analysis of Giant Vesicles. *Soft Matter* **2010**, *6* (7), 1472.  
 913 <https://doi.org/10.1039/b920629a>.
- 914 (39) Xu, H.; Huang, C. H. Scanning Calorimetric Study of Fully Hydrated Asymmetric  
 915 Phosphatidylcholines with One Acyl Chain Twice as Long as the Other. *Biochemistry* **1987**,  
 916 *26* (4), 1036–1043. <https://doi.org/10.1021/bi00378a009>.
- 917 (40) Veatch, S. L.; Keller, S. L. Organization in Lipid Membranes Containing Cholesterol. *Phys.*  
 918 *Rev. Lett.* **2002**, *89* (26), 268101. <https://doi.org/10.1103/PhysRevLett.89.268101>.
- 919 (41) Koynova, R.; Caffrey, M. Phases and Phase Transitions of the Phosphatidylcholines.  
 920 *Biochimica et Biophysica Acta (BBA) - Reviews on Biomembranes* **1998**, *1376* (1), 91–145.  
 921 [https://doi.org/10.1016/S0304-4157\(98\)00006-9](https://doi.org/10.1016/S0304-4157(98)00006-9).
- 922 (42) Davis, P. J.; Keough, K. M. W. Differential Scanning Calorimetric Studies of Aqueous  
 923 Dispersions of Mixtures of Cholesterol with Some Mixed-Acid and Single-Acid  
 924 Phosphatidylcholines. *Biochemistry* **1983**, *22* (26), 6334–6340.  
 925 <https://doi.org/10.1021/bi00295a045>.
- 926 (43) Morales-Pennington, N. F.; Wu, J.; Farkas, E. R.; Goh, S. L.; Konyakhina, T. M.; Zheng, J. Y.;  
 927 Webb, W. W.; Feigenson, G. W. GUV Preparation and Imaging: Minimizing Artifacts.  
 928 *Biochimica et Biophysica Acta (BBA) - Biomembranes* **2010**, *1798* (7), 1324–1332.  
 929 <https://doi.org/10.1016/j.bbamem.2010.03.011>.
- 930 (44) Xin, W.; Wu, H.; Grason, G. M.; Santore, M. M. Switchable Positioning of Plate-like  
 931 Inclusions in Lipid Membranes: Elastically Mediated Interactions of Planar Colloids in 2D  
 932 Fluids. *Sci. Adv.* **2021**, *7* (14), eabf1943. <https://doi.org/10.1126/sciadv.abf1943>.
- 933 (45) Pritzl, S. D.; Urban, P.; Prasselsperger, A.; Konrad, D. B.; Frank, J. A.; Trauner, D.;  
 934 Lohmüller, T. Photolipid Bilayer Permeability Is Controlled by Transient Pore Formation.  
 935 *Langmuir* **2020**, *36* (45), 13509–13515. <https://doi.org/10.1021/acs.langmuir.0c02229>.
- 936 (46) Mabrey, S.; Sturtevant, J. M. Investigation of Phase Transitions of Lipids and Lipid  
 937 Mixtures by Sensitivity Differential Scanning Calorimetry. *Proc. Natl. Acad. Sci. U.S.A.*  
 938 **1976**, *73* (11), 3862–3866. <https://doi.org/10.1073/pnas.73.11.3862>.
- 939 (47) Knorr, R. L.; Steinkühler, J.; Dimova, R. Micron-Sized Domains in Quasi Single-Component  
 940 Giant Vesicles. *Biochimica et Biophysica Acta (BBA) - Biomembranes* **2018**, *1860* (10),  
 941 1957–1964. <https://doi.org/10.1016/j.bbamem.2018.06.015>.
- 942 (48) Bagatolli, L. A.; Gratton, E. Two-Photon Fluorescence Microscopy Observation of Shape  
 943 Changes at the Phase Transition in Phospholipid Giant Unilamellar Vesicles. *Biophysical*  
 944 *Journal* **1999**, *77* (4), 2090–2101. [https://doi.org/10.1016/S0006-3495\(99\)77050-5](https://doi.org/10.1016/S0006-3495(99)77050-5).
- 945 (49) Rosetti, C. M.; Mangiarotti, A.; Wilke, N. Sizes of Lipid Domains: What Do We Know from  
 946 Artificial Lipid Membranes? What Are the Possible Shared Features with Membrane Rafts  
 947 in Cells? *Biochimica et Biophysica Acta (BBA) - Biomembranes* **2017**, *1859* (5), 789–802.  
 948 <https://doi.org/10.1016/j.bbamem.2017.01.030>.
- 949 (50) Wan, H.; Jeon, G.; Xin, W.; Grason, G. M.; Santore, M. M. Flower-Shaped 2D Crystals  
 950 Grown in Curved Fluid Vesicle Membranes. *Nat Commun* **2024**, *15* (1), 3442.  
 951 <https://doi.org/10.1038/s41467-024-47844-x>.
- 952 (51) Veatch, S. L.; Keller, S. L. Separation of Liquid Phases in Giant Vesicles of Ternary Mixtures  
 953 of Phospholipids and Cholesterol. *Biophysical Journal* **2003**, *85* (5), 3074–3083.  
 954 [https://doi.org/10.1016/S0006-3495\(03\)74726-2](https://doi.org/10.1016/S0006-3495(03)74726-2).

- 955 (52) Portet, T.; Gordon, S. E.; Keller, S. L. Increasing Membrane Tension Decreases Miscibility  
956 Temperatures; an Experimental Demonstration via Micropipette Aspiration. *Biophysical*  
957 *Journal* **2012**, *103* (8), L35–L37. <https://doi.org/10.1016/j.bpj.2012.08.061>.
- 958 (53) Uline, M. J.; Schick, M.; Szleifer, I. Phase Behavior of Lipid Bilayers under Tension.  
959 *Biophysical Journal* **2012**, *102* (3), 517–522. <https://doi.org/10.1016/j.bpj.2011.12.050>.
- 960 (54) Urban, P.; Pritzl, S. D.; Ober, M. F.; Dirscherl, C. F.; Pernpeintner, C.; Konrad, D. B.; Frank,  
961 J. A.; Trauner, D.; Nickel, B.; Lohmueller, T. A Lipid Photoswitch Controls Fluidity in  
962 Supported Bilayer Membranes. *Langmuir* **2020**, *36* (10), 2629–2634.  
963 <https://doi.org/10.1021/acs.langmuir.9b02942>.
- 964 (55) Foley, S. L.; Hossein, A.; Deserno, M. Fluid-Gel Coexistence in Lipid Membranes under  
965 Differential Stress. *Biophysical Journal* **2022**, *121* (16), 2997–3009.  
966 <https://doi.org/10.1016/j.bpj.2022.07.021>.
- 967 (56) Reagle, T.; Xie, Y.; Li, Z.; Carnero, W.; Baumgart, T. Methyl- $\beta$ -Cyclodextrin Asymmetrically  
968 Extracts Phospholipid from Bilayers, Granting Tunable Control over Differential Stress in  
969 Lipid Vesicles. *Soft Matter* **2024**, *20* (21), 4291–4307.  
970 <https://doi.org/10.1039/D3SM01772A>.
- 971 (57) Miele, Y.; Holló, G.; Lagzi, I.; Rossi, F. Shape Deformation, Budding and Division of Giant  
972 Vesicles and Artificial Cells: A Review. *Life* **2022**, *12* (6), 841.  
973 <https://doi.org/10.3390/life12060841>.
- 974 (58) Peng, Z.; Iwabuchi, S.; Izumi, K.; Takiguchi, S.; Yamaji, M.; Fujita, S.; Suzuki, H.; Kambara,  
975 F.; Fukasawa, G.; Cooney, A.; Michele, L. D.; Elani, Y.; Matsuura, T.; Kawano, R. Lipid  
976 Vesicle-Based Molecular Robots. *Lab Chip* **2024**, *24* (5), 996–1029.  
977 <https://doi.org/10.1039/D3LC00860F>.  
978

## Supporting Information

### Light-controlled membrane remodeling in gel-fluid phase-separated giant vesicles using photoswitchable lipids

Tsu-Wang Sun<sup>1</sup>, Elias Sabri<sup>1</sup>, Mina Aleksanyan<sup>1</sup>, Rumiana Dimova<sup>1,\*</sup>

<sup>1</sup>Max Planck Institute of Colloids and Interfaces, 14476 Potsdam, Germany

\* Address correspondence to: [Rumiana.Dimova@mpikg.mpg.de](mailto:Rumiana.Dimova@mpikg.mpg.de)

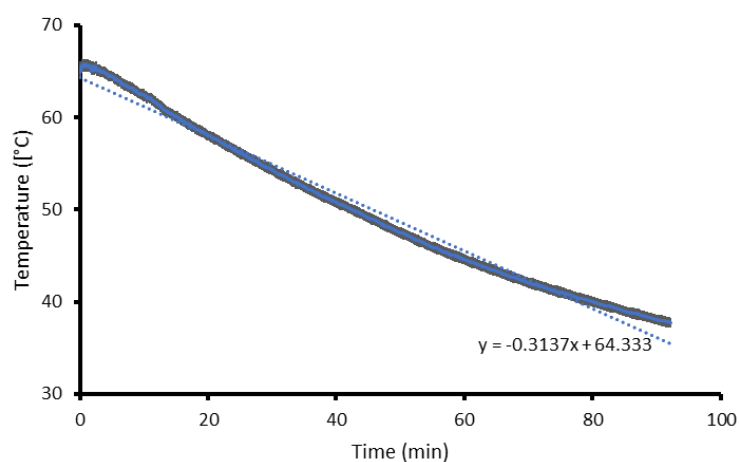


**Figure S1.** Cooling temperature recorded in the oven (where GUVs were electroformed) after switching it off upon completing GUV electroformation. The cooling rate is around 0.3 K/min estimated from the slope of the linear fit (dotted line).

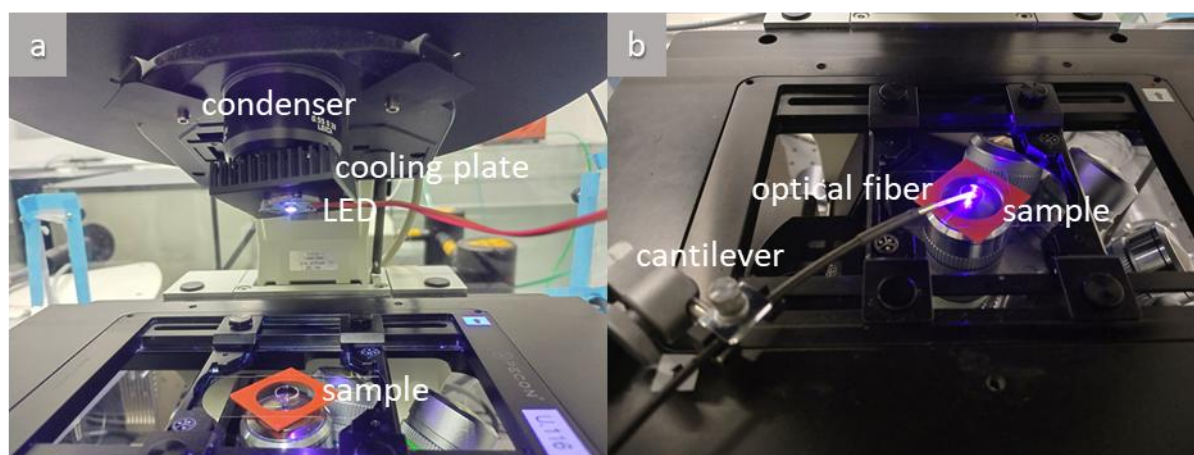


**Figure S2.** Photographs depicting the two approaches used to apply irradiation to the sample: (a) The UV-LED unit is positioned above the sample observation chamber and is attached to the condenser of a microscope (in this picture, the condenser tower is tilted back for better visualization). (b) A fiber-coupled LED system consisting of an optical fiber held by a cantilever over the sample. In both images, the observation chamber is assembled from two coverslips sealed by a Press-to-Seal silicone spacer (red) encircling the sample drop.

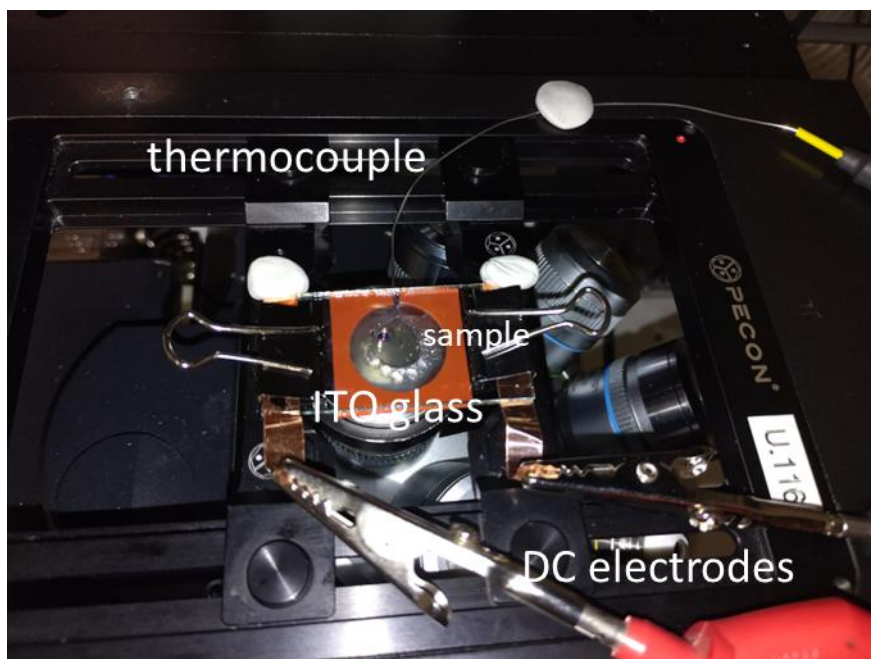


**Figure S3.** Top view photograph of chamber and heating elements for establishing temperature control on GUV samples under the microscope. The detailed sketch of the setup is provided in Fig. S4a in the main text.

### Numerical simulations

Numerical simulations were performed using the finite element method implemented in COMSOL Multiphysics (COMSOL Multiphysics® v. 5.2. www.comsol.com. COMSOL AB, Stockholm, Sweden) on a cluster computer (262 GB RAM, Intel® Xeon® 2.2 GHz (48 CPUs) processor). The model was implemented in a 2D-axisymmetric formulation, as illustrated in Fig. S4a.

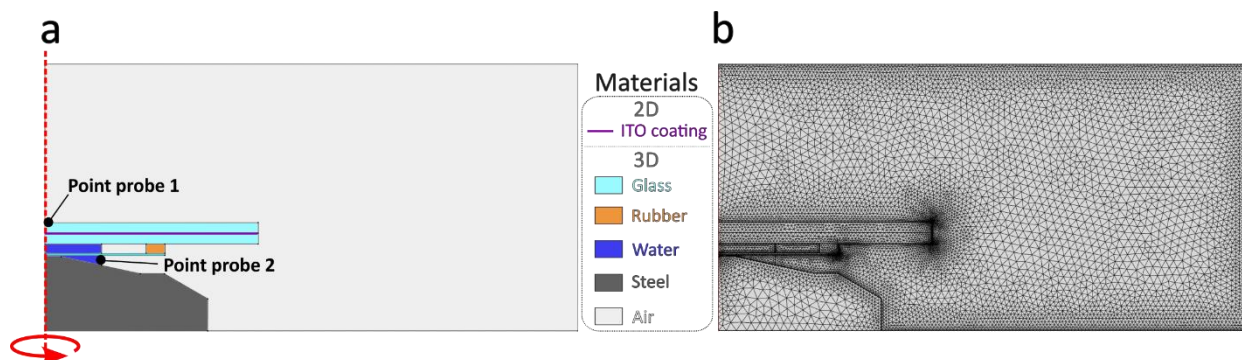


**Figure S4.** Numerical model geometry and mesh. (a) Geometry of the numerical setup. The dimensions of the different parts of the system correspond to those shown in Fig. 4A in the main text and are given in Fig. S9. The red dotted line represents the axis of rotational symmetry. Distinct colored regions represent simulation domains with material properties listed in Table S1. Point probe 1 and point probe 2 refer to the positions at which the two thermocouples were placed (above the top ITO slide and in the space between the objective and coverslip below the chamber) providing values for the respective boundary conditions. (b) Snapshot of the fully meshed computational domain, including refined boundary-layer elements at various interfaces.

The computational domain was discretized using triangular finite elements, with two layers of rectangular boundary-layer elements applied at the fluid interfaces to improve resolution of thermal gradients. A snapshot of the fully meshed geometry is shown in Fig. S4b. The total number of elements in each domain and their corresponding average mesh quality are summarized in Table S1.

In the following, we summarize the sets of equations solved numerically. Values of all material parameters are given in Table S1.

In the fluid domains (water and air in Fig. S4), the following heat transfer equation was solved:

$$\rho C_p \frac{\partial T}{\partial t} + \rho C_p \mathbf{u} \cdot \nabla T + \nabla \cdot \mathbf{q} = 0, \quad (\text{S1})$$

where  $T$  is the temperature,  $\mathbf{q} = -\kappa \nabla T$  is the heat flux with  $\kappa$  the thermal conductivity,  $\nabla$  is the divergence operator,  $C_p$  is the specific heat capacity at constant pressure,  $\mathbf{u}$  is the velocity and  $\rho$  is the density. This equation was coupled to the Navier-Stokes equation under the Boussinesq approximation, such that the density variations were considered only in the buoyancy term  $\rho \mathbf{g}$ , while the fluid was treated as incompressible, i.e.  $\nabla \cdot \mathbf{u} = 0$ . The momentum equation reads:

$$\rho_0 \left( \frac{\partial \mathbf{u}}{\partial t} + \mathbf{u} \cdot \nabla \mathbf{u} \right) = -\nabla p + \mu \nabla^2 \mathbf{u} + \rho_0 \mathbf{g} - \rho_0 \frac{(T-T_0)}{T_0} \mathbf{g}, \quad (\text{S2})$$

where  $p$  is the hydrostatic pressure,  $\mu$  is the fluid viscosity,  $\mathbf{g}$  is the gravitational acceleration vector, and  $T_0$  is the reference temperature, set to 25°C.

In the solid domains (glass, rubber and steel, see Fig. S4a), the heat transfer was modeled by the heat conduction equation:

$$\rho C_p \frac{\partial T}{\partial t} + \nabla \cdot \mathbf{q} = 0 \quad (\text{S3})$$

The following Dirichlet boundary conditions were imposed at the ITO interface between the two glass slides (purple boundary in Fig. S4a) and on the bottom interface of the steel objective domain:

$$T = T_{input} \quad (\text{S4})$$

The imposed temperature  $T_{input}$  was adjusted so that the computed temperatures at the top glass and coverslip bottom positions of the simulated chamber (see point probes 1 and 2 in Fig. S4a) would match the respective experimentally measured temperatures.

Built-in open boundary Dirichlet conditions were imposed at the top, side and bottom air boundaries:

$$T = T_{ref}, \quad (\text{S5})$$

$$-\mathbf{n} \cdot \mathbf{q} = 0, \quad (\text{S6})$$

where  $\mathbf{n}$  represents the interface normal vector and  $T_{ref}$  is the room temperature (set to 23°C). Additionally, no-slip boundary conditions

$$\mathbf{u} = \mathbf{0}, \quad (\text{S7})$$

were applied to the boundaries of all liquid domains (air and water).

**Table S1:** Summary of the computational characteristics and material properties for each domain of the numerical model represented in Fig. S4.

Material	ITO layer	Glass	Rubber	Water	Steel	Air
Number of elements	45	810	87	549	587	6100
Average element quality	1	0.92	0.96	0.58	0.96	0.84
Thermal conductivity $\kappa$ (W.m.K <sup>-1</sup> )	1	1.38	0.25	0.6	44.5	0.024
Specific heat capacity $C_p$ (J.kg <sup>-1</sup> .K <sup>-1</sup> )	341	703	1802	4184	475	1005
Density $\rho$ (kg.m <sup>-3</sup> )	7000	2203	1200	1000	7850	1.225
Viscosity $\mu$ (J.s.m <sup>-3</sup> )	N.A.	N.A.	N.A.	10 <sup>-3</sup>	N.A.	1.8x10 <sup>-5</sup>

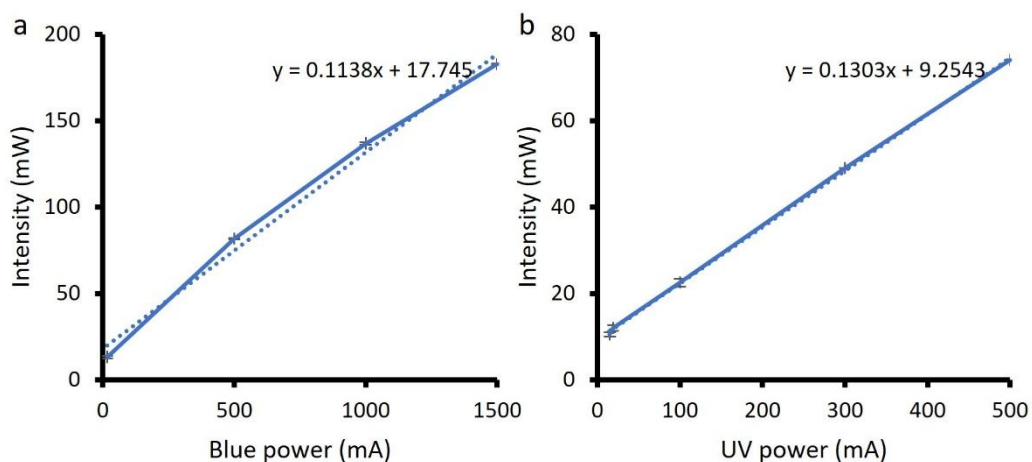


**Figure S5.** Light intensities estimated from (a) blue and (b) UV light fiber-LED device showing the correlation between the setpoint on the device (mA) and the output intensity (mW). The maximum power outputs, measured at the sample plane, were determined using a LaserMate 10 sensor and console (Coherent, USA).

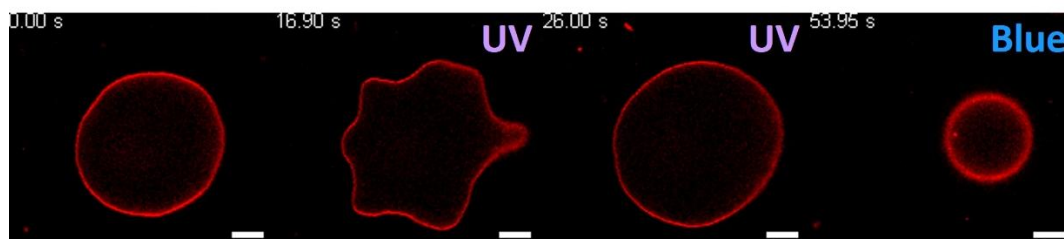


**Figure S6.** Response of fluid azoPC:POPC 1:1 vesicle to UV and blue light irradiation observed under confocal microscopy. The vesicle was irradiated with UV light ( $\sim 170 \text{ mW/cm}^2$ ) undergoes transient budding (second image) relaxing to a floppey vesicle (third image), a process fully reversed with blue light from confocal laser irradiation (last image). Note that because the vesicle has moved vertically, the confocal cross section shows an apparent smaller diameter under blue light. Scale bars:  $10 \mu\text{m}$ .

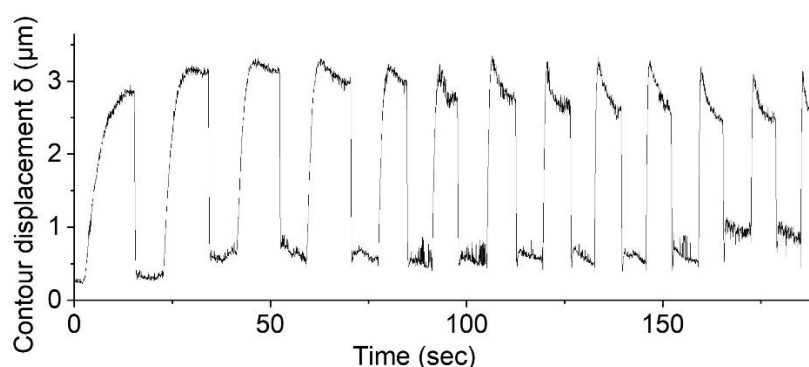


**Figure S7.** Time dependence of the contour deviation (for definition, see Eq. 1 in the main text) of a 1:1 azoPC:DPPC vesicle exposed to UV light (at intensity of 12, 14, 17, 20, 22, 29, 35, 42, 48, 55, 61, 68, and  $74 \text{ mW/cm}^2$ , respectively for the consecutive peaks) and then to blue light (at intensity of  $75 \text{ mW/cm}^2$ ) showing fully reversed shape as demonstrated by the example bright field images in Fig. 1B in the main text and Movie S1. The change in the shape of the peaks plausibly reflects slight rotation of the GUV.

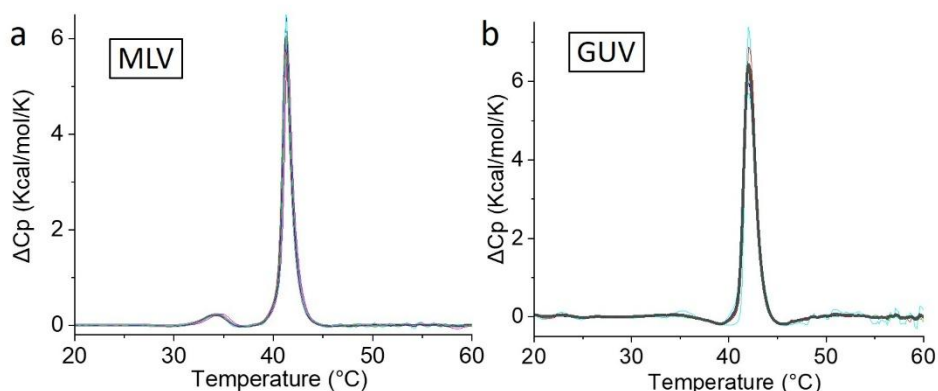


**Figure S8.** DSC heat capacitance curves for DPPC (a) MLVs and (b) GUVs showing main transition peaks at 41.3 °C and 42.0 °C, respectively. The pretransition peak at 34.5°C observed with MLVs is not detected for the GUV sample in which the noise is also stronger. The colored curves represent five consecutive heating scans, with the averaged profile shown as a thick light grey line.

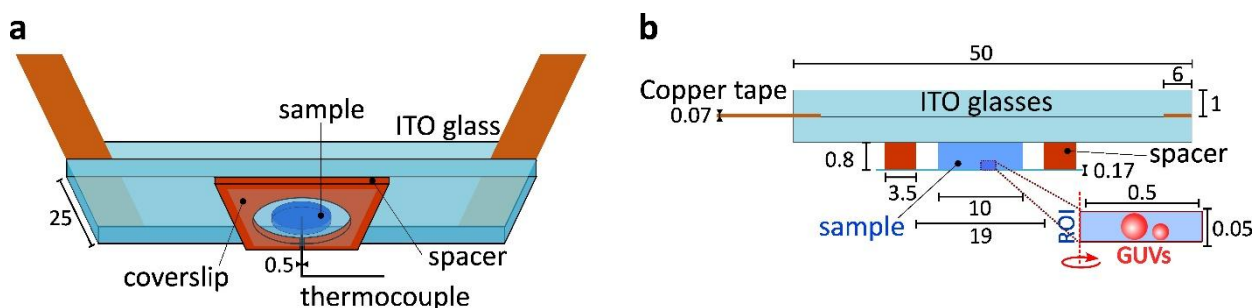


**Figure S9.** Schematic of the temperature-controlled setup in (a) oblique perspective (as shown in Fig. 4 in the main text) and (b) vertical cross-section, the referenced dimensions are in millimeters and are not to scale. The ROI represents the simulated region of interest where the red dashed line represents the axis of rotational symmetry.

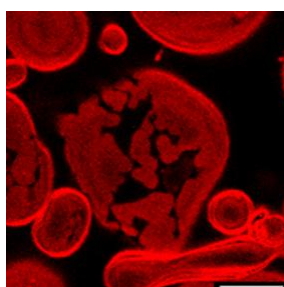


**Figure S10.** Kinetically trapped gel domains during stepwise heating. Confocal fluorescence image of a 1:1 azoPC:DPPC GUV at a sample temperature of 50°C (48±2 simulated). The image was acquired after a stepwise heating protocol (Fig. 5) with approximately 5 minutes of equilibration at each setpoint. Despite the temperature exceeding the main transition, kinetically trapped large gel (dark) domains persist. Scale bar: 10 μm.

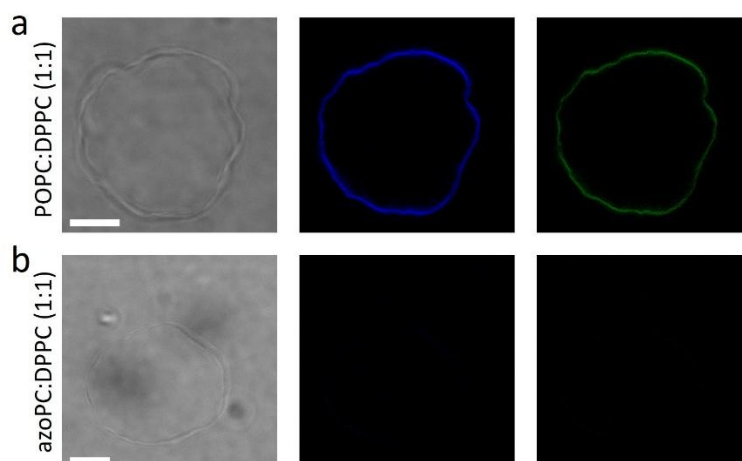
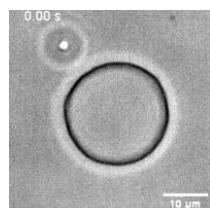


**Figure S11.** Incompatibility of LAURDAN with azoPC-containing membranes. Brightfield and two-photon confocal images of (a) POPC:DPPC (1:1) and (b) azoPC:DPPC (1:1) vesicles containing 0.5 mol% LAURDAN at 23°C. LAURDAN was excited via two-photon excitation at 780 nm. Fluorescence emission was collected in two channels: blue (400–460 nm, middle) and green (470–530 nm, right). In the presence of azoPC (b), LAURDAN fluorescence signal is strongly reduced, likely due to FRET-mediated quenching by the azobenzene moiety. Consistent with this quenching effect, further irradiation with UV or blue light resulted in no detectable morphological changes to the vesicles, indicating a lack of photoswitching-induced membrane area change or LAURDAN-mediated sensitization. Scale bars: 10  $\mu\text{m}$ .

## Movie captions

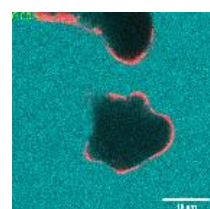


**Movie S1. Reversible global crumpling in a phase-separated 1:1 azoPC:DPPC GUV corresponding to Fig. 1C in the main text.** Brightfield microscopy recording at room temperature. The GUVs were prepared by gradual cooling ( $\sim 0.3$  K/min). Upon UV irradiation ( $\sim 74$  mW/cm<sup>2</sup>), the vesicle undergoes pronounced global crumpling and twisting deformations distributed across the entire membrane surface, reflecting mechanical frustration between the expanding azoPC-rich fluid domains and the rigid

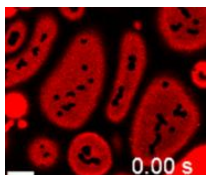
DPPC-rich gel regions that resist uniform area expansion. The crumpled morphology is fully reversed upon blue light irradiation ( $\sim 75$  mW/cm<sup>2</sup>), restoring the original vesicle shape.



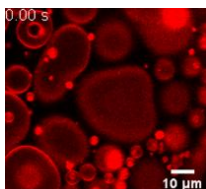
**Movie S2. Reversible localized budding in faceted 1:1 azoPC:DPPC GUVs observed by brightfield microscopy.** Deflated vesicles with coarsened domains at room temperature exhibit flat facets characteristic of rigid DPPC-rich gel regions, which remain immobile throughout irradiation, while the curved fluid segments between them protrude (inward or outward) as localized buds upon UV irradiation ( $\sim 74$  mW/cm<sup>2</sup>). The buds retract fully upon blue light ( $\sim 75$  mW/cm<sup>2</sup>), restoring the original faceted morphology. The sequence corresponds to the behavior illustrated in Fig. 1D.



**Movie S3. Reversible localized budding in coarsened azoPC:DPPC GUVs observed by confocal microscopy.** Confocal fluorescence recording of a deflated azoPC:DPPC (1:1) GUV with coarsened gel domains at room temperature. The membrane is labeled with 0.1 mol% Atto-647N-DOPE (red); sulforhodamine B (SRB, cyan) is present in the external solution at  $\sim 50$   $\mu\text{M}$ . Fluid azoPC-rich domains protrude as localized buds upon UV irradiation ( $\sim 74$  mW/cm<sup>2</sup>), while the surrounding DPPC-rich gel regions remain flat and unperturbed. Full retraction of the buds is observed upon blue light irradiation ( $\sim 75$  mW/cm<sup>2</sup>). The absence of SRB signal inside the vesicle throughout confirms that membrane integrity is preserved during repeated deformation cycles. The sequence corresponds to Fig. 1F.



**Movie S4. Nucleation and coalescence of gel domains upon cooling.** Appearance of small circular gel domains at a sample temperature of 48°C (simulated: 44÷48°C) upon cooling, followed by progressive coalescence of domain boundaries. The sequence corresponds to Fig. 5B.



**Movie S5. Reversible photoinduced domain nucleation in a fully melted azoPC:DPPC membrane.** Small six-lobed gel domains nucleate within a homogeneous fluid membrane at 55°C sample temperature (simulated 51÷55°C) upon UV irradiation at 74 mW/cm<sup>2</sup>, and dissolve fully upon subsequent blue light exposure. One also observes slight area increase of the vesicles under UV light. The sequence corresponds to Fig. 6.